
Foraminiferal sandy contourite of the Limpopo Corridor (Mozambique margin): Facies characterization and paleoceanographic record

Lopes U. ^{6,*}, Babonneau Nathalie ⁶, Fierens R. ⁶, Revillon Sidonie ^{1,2}, Raison F. ³, Miramontes E. ^{4,5}, Rabineau Marina ⁷, Aslanian Daniel ¹, Moulin Maryline ¹

¹ Geo-Ocean, Univ Brest, CNRS, Ifremer, UMR6538, F-29280 Plouzané, France

² SEDISOR, place N. Copernic, 29280 Plouzané, France

³ TotalEnergies, CSTJF, Avenue Larribau, 64000 Pau, France

⁴ MARUM-Center for Marine Environmental Sciences, University of Bremen, Bremen 28359, Germany

⁵ Faculty of Geosciences, University of Bremen, Bremen 28359, Germany

⁶ Geo-Ocean, Univ Brest, CNRS, Ifremer, UMR6538, F-29280 Plouzané, France

⁷ Geo-Ocean, Univ Brest, CNRS, Ifremer, UMR6538, F-29280 Plouzané, France

* Corresponding author : U. Lopes, email address : lopes-ugo@hotmail.fr

Abstract :

Contourites encompass a wide variety of sedimentary facies. Some of them show common facies with others deep-water deposits, such as turbidites and hemipelagites. Sedimentological characterization at macro- and microscales is valuable to discriminate those close facies but the distinction is not always clear. Contourites are increasingly used in paleoceanographic and paleoclimatic reconstructions. Improving their characterization is therefore essential to their interpretations.

This study aims at characterizing a foraminiferal sandy contourite facies from a sediment core collected on top of a contourite drift under the influence of the Antarctic Intermediate Water/North Atlantic Deep-Water interface located in the Limpopo Corridor (Mozambique margin, Indian Ocean) at 2000 m depth. This work is based on a detailed analysis of the sedimentary record using physical properties (gamma density and magnetic susceptibility) as well as laser grain size and X-Ray Fluorescence core scanning data.

Our results show that: (1) the foraminiferal sand is vertically continuous and homogenous over 633 kyr with an average sedimentation rate of 0.26 cm.kyr⁻¹; (2) this contourite facies results from sedimentation with low terrigenous inputs under stable hydrodynamic conditions over time, with relatively strong bottom currents for this water depth (~16 cm.s⁻¹); (3) during glacial stages, sedimentation rates are lower and bottom current speed is higher than during interglacial stages. We also propose the concept of “Contourite Graphical Chart” which summarizes the theoretical distribution of contourite endmembers from cross-plot of “sorting versus grain-size median D50” and their related sedimentary processes. This study highlights the relevance of condensed foraminiferal sandy contourites as long time-scale paleoceanographic archives and provides new insights for studies related to paleoclimatology and paleoecology.

Highlights

► Continuous and homogeneous foraminiferal sandy contourite facies. ► Very low sedimentation rate of 0.26 cm.kyr^{-1} . ► This sedimentary facies results from the action of strong bottom currents related to the AAIW/NADW interface. ► Bottom current speed increases during glacial stages and decreases during interglacial stages.

Keywords : Bottom current, Contourite Foraminiferal sand, Paleoceanography, Mozambique Channel, Indian Ocean, Quaternary

1. INTRODUCTION

Contourites are sediments deposited or significantly affected by the action of bottom currents (Stow et al., 2002; Rebesco, 2005; Stow and Faugères, 2008). Their accumulations, i.e., contourite drifts and related erosional features, i.e., contourite channels, moats and furrows, form large sedimentary structures on continental margins called contourite depositional systems (Hernández-Molina et al., 2003). Since their discovery in the 1960s (Heezen and Hollister, 1964; Hollister, 1967), contourite drifts have raised a growing interest for their applications in the petroleum industry as potential reservoir (e.g., Viana and Rebesco, 2007; Sansom, 2018; Fonnesu et al., 2020; Yu et al., 2020), paleoclimatic and paleoceanographic studies as high resolution sedimentary records (e.g., Knutz, 2008; Miramontes et al., 2016; Tallobre et al., 2017; Gruetzner et al., 2019; Martorelli et al., 2021), sequence stratigraphy and slope instability for their influence on continental margin morphologies (e.g., Brackenridge et al., 2011; Mosher et al., 2017; Miramontes et al., 2018). At large scale, morphological features and internal structures of contourite drifts are well recognized from seismic profiles and bathymetric data, but at macro- and microscale, discrimination of contourites from other deep-water sedimentary deposits is still challenging.

Contourites are part of a sedimentary continuum from continental shelves to deep-sea basins (summarized in Stow and Smillie, 2020). Therefore, contourites are often associated or mixed with other sedimentary deposits like turbidites, hemipelagites or debrites (Rebesco et al., 2008). To establish clear criteria to distinguish contourites, most of the recent studies highlight the usefulness of sediment characterization according to their grain-size parameters (i.e., grain-size indicators such as D_{50} , sorting, skewness, kurtosis), principal component analysis and their microstructural features (Brackenridge et al., 2018; Bankole et al., 2021; de Castro et al., 2020, 2021a, b; Rodrigues et al., 2022). These studies provided useful tools to discriminate contourites from other deep-water deposits, and need to be complemented by further work on lesser-known contourites to obtain a comprehensive understanding.

The Atlantic-Indian Ocean gateway is a key element of the global ocean thermohaline circulation (de Ruijter et al., 1999; Sloyan and Rintoul, 2001). It constitutes an exchange area where warm Indian Ocean surface waters enter the Atlantic Ocean and with the volume lost are compensated at depth by

the influx of North Atlantic Deep Water (NADW) and Antarctic Bottom Water (AABW). The seismic study of Gruetzner et al. (2019) on a contourite drift from the Agulhas Plateau (South Africa, Fig.1) has shown that the most important global climate and oceanographic changes of the last 7 Ma can be recorded in contourite drift sedimentation and used to understand the regional bottom current paleo-variability. In that study area, only two studies have explored the behavior of bottom currents over the last 200 kyr (Molyneux et al., 2007; Krueger et al., 2012) and suggest an increase of NADW during glacial stages.

To the north-east of the Agulhas Plateau, the Mozambique Channel hosts a huge diversity of contourite systems and provides a good area for the study of contourite deposits and bottom current behavior over the Plio-Quaternary (Breitzke et al., 2017; Counts et al., 2018; Thiéblemont et al., 2019, 2020; de Castro et al., 2021b; Evain et al., 2021; Miramontes et al., 2019, 2020, 2021; Babonneau et al., 2022). In the scope of the Passive Margins Exploration Laboratories project (PAMELA), the PAMELA-MOZ3 cruise (Moulin and Aslanian, 2016) has acquired five piston cores (MOZ3-CS03, CS02, CS07, CS06 and CS05) in a contourite system located in the Limpopo Corridor (Figs. 1 and 2). Recent results of Babonneau et al. (2022) on this contourite system have highlighted the existence of a contourite facies composed of foraminiferal sand covering the 11.47 m length of core MOZ3-CS07. Based on two strontium dating at 6 and 11 m, the foraminiferal sand seems to be continuous and condensed over 5 Ma with very low sedimentation rate about 0.3 cm.kyr^{-1} and without influence of gravity deposits or erosional features (Fig. 3). Therefore, this sedimentary succession could provide a good record for Plio-Quaternary paleoceanographic/paleoclimatic reconstructions and contourite characterization.

Bioclastic contourite, and in particular foraminiferal sandy facies, are very poorly known. Some studies mention their existence within contourite systems (Lonsdale and Malfait, 1974; Huizhang and McCave, 1990; Robinson and McCave, 1994; Mulder et al., 2019), but none of them has really studied their characteristics and their depositional processes in depth. However, it is frequently observed in outcrops within fossilized contourites (Schiller et al., 1994; Carter, 2007; Hüneke et al., 2021; Hernández-Molina et al., 2022).

This study is a continuation of the work of Babonneau et al. (2022) with three objectives: (1) improve the knowledge on foraminiferal sandy contourite using physical, geochemical and grain-size

analyses on core MOZ3-CS07; (2) compare characteristics of the foraminiferal sandy contourite facies with other sandy facies found in the same contourite system; and (3) explore its potential as sedimentary record of paleoceanographic changes.

2. REGIONAL SETTING

2.1. Geodynamic setting

The Mozambique Basin is located in the south-west of the Indian Ocean, between Africa and Madagascar (Fig. 1). Its formation results from the breakup of Gondwana and the southwards movement of eastern Gondwana (i.e., Madagascar, India, Australia and Antarctica) in respect to the western Gondwana (South America and Africa) during the Jurassic (Thompson et al., 2019). The Mozambique Basin is fringed to the east by the Davie Fracture Zone (DFZ), which marks the dextral southward movement of Madagascar in respect to Africa between 155 Ma and 120 Ma (Fig. 1). To the west, the Mozambique Fracture Zone (MFZ) marks the southward drift of the Antarctica plate (Watkeys and Sokoutis, 1998; Jokat et al., 2003; Gradstein et al., 2012; Leinweber et al., 2013; Thompson et al., 2019). The southern part of the Mozambique Channel hosts two major topographic highs (Fig. 1): the Mozambique Ridge to the West (MozR) and the Madagascar Ridge to the East (MadR).

The western part of the Mozambique Channel, the Limpopo Corridor, is marked by high positive gravity anomalies (e.g., Mueller and Jokat, 2017) but recent data acquired during the PAMELA project showed that these anomalies are related to large and thick contourite drifts above a thin continental intruded crust (Moulin et al., 2020; Evain et al., 2021; Li et al., 2021; Matsinhe et al., 2021).

The Limpopo Corridor corresponds to a strike-slip or slightly transtensional margin, where the MFZ marks the continent-ocean transition (Evain et al., 2021).

2.2. Oceanographic and morpho-sedimentary setting

The ocean circulation within the Mozambique Channel is constrained by its complex and incised morphology. The warm and surface water masses (>1200 m) coming from the northern Indian Ocean and the Red Sea, constitute the Mozambique Current (MC) and flow preferentially southward along the African coast (Fig. 1). Conversely, the intermediate and deep-water masses from the Atlantic (North

Atlantic Deep Water "NADW" 2200-3500 m) and Antarctic (Antarctic Intermediate Water "AAIW" 800-1500 m and Antarctic Bottom Water "AABW" >4000 m) flow northwards (de Ruijter et al., 2002; Ullgren et al., 2012; Miramontes et al., 2019). Bottom currents strongly interact with the seafloor and their circulation is impacted by the submarine reliefs. The AABW and part of the NADW are thus redirected in a southward rip current to meet the shoals of the Northern Mozambique Basin (Fig. 1; van Aken et al., 2004; Miramontes et al., 2019). The oceanographic circulation in the Mozambique Channel is also affected by large oceanic eddies coming from the north and the east, flowing southward along the African margin. These eddies are known to impact the seafloor until 3000 meters below the sea-level (mbsl; Fig. 1; Sætre and da Silva, 1984; Swart et al., 2010; Halo et al., 2014).

Thiéblemont et al. (2019) mapped the contourite depositional system of the Limpopo Corridor. Their results show four contourite terraces, and they propose as the main factors for the formation of these contourite terraces, the internal waves of tidal period generated at the transition zone between two water masses.

Gao et al. (2020) and Thiéblemont et al. (2020), confirmed the influence of water mass circulation and their interactions on the shaping of the African margin. Using seismic reflection data acquired in the northern Mozambique margin, their work shows the morpho-sedimentary evolution of the ridge since the Cretaceous in relation to changes in global ocean circulation. They defined four stages of sedimentary construction: (1) Lower Cretaceous, development of progradational clinoforms with hemipelagite drape after the initial break-up phase; (2) Upper Cretaceous, development of the first contourite system; (3) Paleocene-Eocene, sedimentation dominated by gravity processes; (4) Middle Miocene, re-establishment of contourite systems in the lower part of the continental slope with the formation of the various present contourite terraces.

2.3. Contourite system studied

The study area is characterized by the presence of a contourite system located in the Limpopo Corridor between 1800 and 2200 mbsl (Fig. 1). It is 75 km long and 50 km wide, with a NNE-SSW orientation. The system is divided into two mounded drifts, surrounded by two main channels on the eastern and western edges, separated by an intermediate channel (Fig. 2A). According to the closest

water mass depths measurement from our study area (Thiéblemont et al., 2019; Gao et al., 2020), the present contourite system is located at the transition zone between the base of the AAIW (1500 mbsl) and the top of the NADW (2200 mbsl; both flowing northward) corresponding to a progressive change in seawater density about 700 m thick (Thiéblemont et al., 2019).

Babonneau et al. (2022) studied the sedimentary architecture of the contourite system since the Cretaceous based on seismic profile and its recent behavior through stratigraphic correlations from sediment cores. The contourite drift evolution shows three stages of construction (Fig. 3): (1) initiation and development of the drift/channel system from the Cretaceous to the Miocene; (2) an intermediate stage with successive incisions/aggradations, and; (3) channel infill and drift erosion since the Plio-Quaternary. The depositional process of the contourite system during the stage 3 is explained by the lateral and vertical change in the area of high current speed and by the morphological evolution of the system itself. This stage of channel filling is also recognized by Thiéblemont et al. (2020) and interpreted as resulting from the onset of NADW and AAIW in the Southern Hemisphere during the middle Miocene, which significantly changed the water circulation along the Mozambique margin.

Since the Plio-Quaternary, the drift growth has stopped. Low sedimentation rates of 3 to 1.9 cm.kyr⁻¹ are recorded in the western channel, and about 0.3 cm.kyr⁻¹ on the western flank of the drift. The top and the eastern flank of the drift are in erosion. The sedimentary facies vary from the western to the eastern part of the contourite system, with mixed siliciclastic-bioclastic sediments (clay to fine-sand in grain size) in the western channel, transitioning into pelagic-sourced bioclastic sands (foraminifers dominated) near the top of the drift (Fig. 3).

3. MATERIALS AND METHODS

3.1. Bathymetry and sediment cores

Five Calypso piston cores (Figs. 2 and 3) were collected on the contourite system during the PAMELA-MOZ3 oceanographic cruise aboard the R/V "Pourquoi pas?" (Moulin and Aslanian, 2016) at water depths ranging from 1853 to 2125 mbsl (Table 1 and Fig. 2). All the data acquired on the piston cores are summarized in Table 2.

The regional bathymetric map (Fig. 1) is the "General Bathymetric Chart of the Ocean" (GEBCO_08, version 2010-09-27, <http://www.gebco.net>). The detailed bathymetry (Figs. 2A and 2B) is acquired with a multibeam echosounder (SMF) ©RESON-Seabat 7150 bi-frequency 12/24 kHz, allowing the acquisition of reflectivity images and the bathymetry of the seafloor with 20x20m resolution grid. The MOZ3-SDS-0038 seismic profile (Fig. 2C) was acquired with a CHIRP sediment echosounder with a signal frequency varying between 5300 and 1800 Hz, allowing for ~80 m penetration into the sediment with an average resolution of 0.75 m.

3.2. X-Ray Fluorescence (XRF) core scanner and Multi-Sensor Core Logger (MSCL) data

X-Ray Fluorescence (XRF) measurements are used to analyze the variations of the geochemical composition of the sediment. XRF measurements were performed at a 1 cm interval with the Avaatech X-Ray Core Scanner from Ifremer on split cores. Two energy sources were used (10 and 30 kv at 0.6 mA and 1 mA) to measure the semi-quantitative value (in count per second) of more than 25 elements having an atomic mass between aluminum and uranium. Among them, we use the log-normalized ratios $\ln(\text{Ca/Fe})$ and $\ln(\text{Zr/Rb})$ as a respective indicator of the terrigenous versus biogenic sediment proportion and as an indicator of the bottom current intensity (Weltje and Tjallingii, 2008; Vandorpe et al., 2019; Wu et al., 2020).

Physical parameters (gamma-density and magnetic susceptibility) were acquired with a Multi-Sensor Core-Logger (MSCL Geotek Ltd) at Ifremer (Brest), with a sampling interval of 1 cm. X-ray radiography (CT scan, Geotek Ltd) was also acquired on the core half-sections at Ifremer (Brest).

3.3. Grain-size analysis

Laser grain-size measurements were performed on bulk sediment with the ©Malvern 2000G from UMR Geo-Ocean (Brest) giving an accurate measurement of particles with a size from 0.02 to 2000 μm . A total of 907 measurements were performed on cores MOZ3-CS03, MOZ3-CS02, MOZ3-CS07 and MOZ3-CS06. On the cores MOZ3-CS03, MOZ3-CS02 and MOZ3-CS06, measurements were performed on selected parts (most frequently on coarser intervals), whereas on MOZ3-CS07, sampling resolution ranges from 1 to 3 cm and is defined according to the $\ln(\text{Ca/Fe})$ and $\ln(\text{Zr/Rb})$ curves. For all core

samples, ~10 mg of sediment was collected over a 5 mm width, placed in distilled water for 24 hours and vibrated during 4 minutes to deflocculate the particles before laser grain-size measurement.

The grain-size data were processed with the GRADISTAT program (Blott and Pye, 2001). The grain-size indicators (sorting, skewness and D_{50}) were calculated using the method of Folk and Ward (1957). The grain-size fractions used are those defined by Friedman and Sanders (1978). The use of cross-plots "skewness versus D_{50} " and "sorting versus D_{50} " provides the characterization of the grain-size sorting evolution and grain-size distribution trend as a function of the increase of the D_{50} for each sample (Blott and Pye, 2001).

3.4. Microfacies

Microfacies analyses were performed at TotalEnergies Scientific and Technical Center (Pau) with Qemscan® technology, which allows inventory, mapping and particle count on the sections. A total of twelve thin sections were analyzed and collected for the core MOZ3-CS07 (Table 3). For each section, the proportion of quartz, feldspar, carbonate, clay and mica, as well as unidentified elements ("Others"), is given. Bulk quantitative mineralogy (BQM) analysis, including elementary composition by DX, density, insoluble residue, loss on ignition (LOI) and cation exchange capacity (CEC) measurements were carried out in addition on 4 of these samples for calibration. Qemscan® and BQM analysis diverge slightly in a few cases (heavy minerals, quartz content).

3.5. Isotopic stratigraphy

Oxygen isotope ($\delta^{18}\text{O}$) measurements were performed on planktonic foraminifers, *Globigerinoides ruber*. On core MOZ3-CS07, 233 samples were collected from 1 to 4.93 meters below the seafloor (mbsf) with the same resolution as grain-size measurements (Table 2). On average, for each sample, 12 specimens were picked (representing 60-120 μg) in the fraction $>250 \mu\text{m}$ and analyzed using the MAT253-KIEL IV isotope ratio mass spectrometer at the IUEM (Brest). Samples are normalized with a standard routine MNHN (V-PDB=-1.93 and std=0.03) and with the international carbonate standards NBS-18=-23.20 and NBS-19=-2.20. The analytical precision is $< 0.05\text{‰}$.

To complete the oxygen isotope measurements, 38 new strontium isotope measurements were performed between 3.51 and 11.45 mbsf (Table 2 and 4) using the Sr Isotope Stratigraphy method (SIS;

Elderfield, 1968; McArthur, 1994). Samples (foraminifer tests or bulk material) are dissolved in weak acetic acid. After centrifugation and evaporation to dryness, dry residues are taken up into 1 ml of HNO₃ 1M and centrifuged before loading on Biorad® columns using Triskem® Sr resin (Pin and Santos Zalduegui, 1997). Sr is eluted in 2 ml of hot ultrapure H₂O. Samples are loaded on W filaments for thermal ionization mass spectrometry (TIMS) measurements. Sr isotope compositions were measured in static mode on a Thermo TRITON at the PSO (Pôle de Spectrométrie Océan) in Brest, France. All measured ratios are normalized to $^{86}\text{Sr}/^{88}\text{Sr}=0.1194$ and the Sr isotope compositions of standard solution NBS987 is routinely measured with a frequency of one full analysis each five samples. Six measurements were made on bulk sediment and 34 measurements were made on the fraction >250 μm (Table 4) to remove as much as possible the detrital sediments and keep exclusively the carbonates, composed mainly of foraminiferal tests.

4. RESULTS

4.1. *Facies and sedimentological characteristics*

4.1.1. *Facies*

Core MOZ3-CS07 presents a single homogenous sedimentary facies, beige, composed of 76.5% fine sand (mostly foraminifers), 19.9% silt and 3.6% clay (Fig. 4). The facies is slightly bioturbated, lamination is difficult to discern (Fig. 5). On the X-ray images, pseudo-cross-bedding can be seen in the lower part of the core (at 9 and 10 mbsf, Fig. 4). Despite being mainly homogenous, the facies of core MOZ3-CS07 shows two variations: (1) foraminiferal pockets, corresponding to lighter intervals with coarser sediments, low content of fine particles and present mainly in the upper part of the core; (2) very fine mottled sand, corresponding to darker intervals with finer sediments, characterized by the presence of black spots (reduced organic matter) and a higher proportion of clay (Figs. 4 and 5).

The magnetic susceptibility and gamma density curves indicate similar trends, with values ranging respectively from 5 to 22 SI⁻¹ and from 1.4 to 1.8 g.cm⁻³ (Fig. 4). Magnetic susceptibility shows an increase from the base of the core to 7.5 mbsf, then a progressive decrease to the top of the core with higher variations. Gamma density shows a progressive decrease from the bottom to the top of the core

that appears to be related to the increase in grain size indicated by a decrease in clays and silts and an increase in sands and D_{50} (Fig. 4).

The $\ln(\text{Ca/Fe})$ ratio reveals an increase in the amount of terrigenous sediment from the base to 8 mbsf, followed by a progressive increase in the amount of biogenic sediment to the top of the core. The $\ln(\text{Zr/Rb})$ ratio indicates a slight increase in current intensity during deposition according to the increase in grain size described above. In general, an increase in the proportion of biogenic sediments and current intensity is observed during the facies formation.

4.1.2. Composition and microfacies

Based on microfacies analyses, the sediment is defined as a foraminiferal calcarenite with a small proportion of silty-clayey mud. The proportion of carbonates varies between 60 and 76%, and the proportion of clay and mica between 6 and 12% (Table 3). The other minerals (i.e., quartz and feldspar) are less abundant and represent between 1.8 and 10% of the sediment.

The detailed description of section 3 (Fig. 5) illustrates the general sedimentary facies composition of core MOZ3-CS07. The X-ray images and photography show a homogenous sediment with no or unclear erosional structures and bioturbation traces. The very fine mottled sands are systematically marked by an increase in gamma density, magnetic susceptibility, clays and silts (corresponding to silty-clayey mud) and by a decrease in D_{50} , and conversely for the foraminiferal pockets. The proportion of silty-clayey mud varies between 10 and 40%. The sample taken at 2.36 mbsf is composed of 62.8% carbonates, 24.5% clay and mica, 7.8% feldspar and 3.7% quartz (Fig. 5B).

4.2. Grain-size analysis of core MOZ3-CS07

4.2.1. Grain-size distribution

Grain-size measurements on core MOZ3-CS07 provide an average grain-size distribution (Fig. 6) that corresponds to a coarse silty sand sediment, very poorly sorted and finely skewed. On average, the mean grain size is 157 μm , the D_{50} is at 344 μm , and the grain-size distribution is unimodal with a mode at 598 μm . Nevertheless, two other peaks not considered as modes are observable at 3 and 100 μm . The general shape of the grain-size distribution allows us to divide it into two major fractions: (1) the fraction $>30 \mu\text{m}$, corresponds to 80% of the sediment, it is composed mostly of foraminifer tests and

in lesser proportion of quartz grains, feldspar and fragmented or juvenile foraminifer tests (Qemscan analysis, Fig. 6); (2) the fraction $<30\ \mu\text{m}$, corresponds to 20% of the sediment, represented by a silty-clayey mud composed of clays and micas.

4.2.2. Grain-size modes

The grain-size distributions of the samples are characterized according to their number of modes. Four types of grain-size distributions are identified with the GRADISTAT program (Fig. 7):

-unimodal distributions, characterized by low variance and a major mode at $600\ \mu\text{m}$. The curves also show two other peaks not considered as grain-size modes at 3 and $100\ \mu\text{m}$.

-bimodal distributions, with mode 1 also located at $600\ \mu\text{m}$ and mode 2 between 2 and $3\ \mu\text{m}$. Some distributions, such as the red curve in figure 7, show modes 1 and 2 in the fraction $>30\ \mu\text{m}$ at 500 and $100\ \mu\text{m}$ respectively.

-trimodal distributions, with mode 1 around $500\ \mu\text{m}$, modes 2 and 3 are located either in the fraction $<30\ \mu\text{m}$ or in the fraction $>30\ \mu\text{m}$.

-quadrимodal distributions show a high diversity of grain-size distributions. On average, mode 1 mostly corresponds to 500 - $600\ \mu\text{m}$, mode 2 to $100\ \mu\text{m}$, mode 3 to $3\ \mu\text{m}$ and the fourth mode to $20\ \mu\text{m}$.

The unimodal and bimodal distributions are the most represented, with 230 and 216 samples, respectively. The proportion of the fraction $<30\ \mu\text{m}$ increases significantly between the unimodal and bimodal distributions from 12.9% to 25.3% and is approximately the same for the trimodal and quadrимodal distributions with respectively 27.5% and 27.2%. The frequency of occurrence of unimodal distributions increases towards the top of the core and is correlated with sand enrichment during deposition (Fig. 4). The other distributions are observed rather in the lower part of the core.

4.2.3. Sorting/Skewness versus D_{50}

The cross-plot of "skewness versus D_{50} " shows two trends: (1) for bimodal, trimodal, and quadrимodal distributions, as D_{50} increases, skewness increases; (2) for unimodal distributions, as D_{50} increases, skewness decreases. Thus, for bimodal, trimodal, and quadrимodal distributions, an increase in D_{50} results in a higher deviation of the distribution toward fine particles, and thus a larger proportion

of the fraction $<30\ \mu\text{m}$. Conversely, for unimodal distributions, the larger the grain size is, the more symmetrical the grain-size distribution is, and the lower the fraction $<30\ \mu\text{m}$ is.

Two trends in sorting are also observed: (1) for bimodal, trimodal, and quadrimodal distributions, there is no clear relationship between D_{50} and sorting; (2) for unimodal distributions, there is an increase in sorting as D_{50} increases. The most poorly sorted sediments are those with bimodal, trimodal and quadrimodal distributions. For unimodal distributions, there is a progressive increase in sorting as D_{50} increases. A trend can be defined that the coarser the grain size is, the fewer the modes are and the better the sediment is sorted.

For both cross-plots shown in figure 8, the transition zone between the two trends for bimodal and unimodal distributions suggests that some bimodal distributions could be reinterpreted as unimodal and *vice versa*.

4.3. Grain-size comparison with the other cores

To complete the characterization of the sedimentary facies from cores MOZ3-CS03, MOZ3-CS02, MOZ3-CS07 and MOZ3-CS06 performed by Babonneau et al. (2022), the grain-size samples are analyzed using a cross-plot of "sorting versus D_{50} " (Fig. 9).

The sediments of core MOZ3-CS07 (yellow points, Fig. 9) form a continuous point cloud ranging from a very poorly sorted sediment with a D_{50} of $70\ \mu\text{m}$ to a moderately well sorted sediment with a D_{50} of $700\ \mu\text{m}$. The sediments of core MOZ3-CS03 (green points) are more diffuse, but broadly divided between a point cloud showing very poorly sorted and very fine sediment with a D_{50} ranging from 7 to $70\ \mu\text{m}$ and a second point cloud showing moderately sorted to moderately well sorted sediments with a D_{50} around $140\ \mu\text{m}$. The sediments of core MOZ3-CS02 (blue points) mark the transition between the point clouds of MOZ3-CS03 and MOZ3-CS07. For moderately sorted to moderately well sorted sediments, the points of MOZ3-CS02 correspond to the sediments with the highest D_{50} , at $900\ \mu\text{m}$. Finally, 12 laser grain-size measurements were performed in the foraminiferal sand and muddy sediments of core MOZ3-CS06 (red points in Fig. 9). These measurements belong to the best sorted and coarsest sediments for the foraminiferal sand and the worst sorted and finest points for the muddy sediments.

Figure 10 shows the mean grain-size distribution and the mineral composition for the four sedimentological poles of the figure 9 called; “Mainly terrigenous”, “Mainly biogenic”, “Siliciclastic sand” and “Foraminiferal sand” after interpretation. The mineral composition of each grain-size mode (Fig. 10) is determined from Qemscan analysis.

-The pole “Mainly terrigenous” based on samples from the core MOZ3-CS03, shows a bimodal distribution with the mode 1 at 4 μm composed of clay and mica, representing 50% of the sediment; the mode 2 at 70 μm composed of quartz and feldspar representing 40% of the sediment and a peak at 400 μm composed of foraminifer tests representing 10% of the sediment.

-The pole “Mainly biogenic” based on samples from the cores MOZ3-CS07 and MOZ3-CS02, reveals a bimodal distribution with the mode 1 at 400 μm mainly composed of foraminifer tests and in lesser proportion of quartz and feldspar, representing 75% of the sediment and; the mode 2 at 3 μm composed of clay and mica, representing 25% of the sediment.

-The pole “Siliciclastic sand” based on samples from the cores MOZ3-CS03 and MOZ3-CS02, shows an unimodal distribution with a mode at 140 μm composed of quartz and feldspar, representing 95% of the sediment and; a peak at 20 μm composed of mica, representing 5% of the sediment.

-The pole “Foraminiferal sand” based on samples from the cores MOZ3-CS07 and MOZ3-CS02, has an unimodal distribution with a mode at 750 μm composed of foraminifer tests, representing 87% of the sediment; a peak at 100 μm composed of quartz and feldspar, representing 5% of the sediment and; a large peak at 6 μm composed of clay and mica, representing 8% of the sediment.

4.4. Isotopic stratigraphy of core MOZ3-CS07

The isotopic stratigraphy of core MOZ3-CS07 is based on $\delta^{18}\text{O}$ measurements correlated with the reference $\delta^{18}\text{O}$ curve LR04 (Lisiecki and Raymo, 2005, Fig. 11) over the first 5 mbsf. This stratigraphy is completed with strontium isotope measurements translated into ages using the global strontium variation reference curve (McArthur et al., 2012) from 3.51 to 11.45 mbsf. The obtained ages are grouped and fitted according to a power regression to better approximate a model of non-linear sedimentation rate evolution over time (Fig. 12).

4.4.1. Oxygen isotopic stratigraphy

The $\delta^{18}\text{O}$ measurements acquired along the first 5 mbsf of core MOZ3-CS07 vary from 0.1 to 1.5 ‰. The $\delta^{18}\text{O}$ curve can be divided into two parts (Fig. 11): (1) from 0 to 1.53 mbsf, the $\delta^{18}\text{O}$ curve shows high-amplitude variations; (2) from 1.53 to 5 mbsf, the $\delta^{18}\text{O}$ curve shows shorter wavelength and lower amplitude changes, with one major peak at 3.7 mbsf.

Over the first 1.53 m, the $\delta^{18}\text{O}$ curve of MOZ3-CS07 correlates with the first 11.5 m of MOZ3-CS03 (Babonneau et al., 2022) and corresponds to the LR04 reference curve to 100 kyr climate cycles (Lisiecki and Raymo, 2005). Sixteen isotopic stages are identified along this part. The first 1.53 m of core MOZ3-CS07 and the 11.5 m of MOZ3-CS03 are estimated to cover the last 632 kyr, with average sedimentation rates respectively about 0.24 cm.kyr^{-1} and 1.82 cm.kyr^{-1} . Sedimentation rate of core MOZ3-CS07 is therefore calculated 7.6 times lower than that of MOZ3-CS03.

Given the sedimentary record resolutions of cores MOZ3-CS07 and MOZ3-CS03, interglacial phases of the last 800 kyr (Past Interglacials Working Group of PAGES, 2015) cannot be distinguished. Therefore, complete odd-numbered MIS (except MIS 3) are labelled as interglacial stages, being aware that they include more than the interglacial phases themselves. The $\delta^{18}\text{O}$ curves of cores MOZ3-CS07 and MOZ3-CS03 thus show interglacial stages that are expressed over thicker sedimentary intervals than glacial stages (in proportion to their actual duration). The $\ln(\text{Ca}/\text{Fe})$ and $\ln(\text{Zr}/\text{Rb})$ ratio of core MOZ3-CS07 reveal an increase in the amount of terrigenous sediment and a decrease in current speed during interglacial stages and conversely during glacial stages.

At 1.53 mbsf in core MOZ3-CS07, the change in the frequency of $\delta^{18}\text{O}$ oscillations is interpreted to mark the end of the Mid-Pleistocene Transition (MPT). Below this level, grain-size proxies the sampling resolution is no longer adapted to the change in frequency and does not allow us to assign an isotopic stage with variations of the $\delta^{18}\text{O}$ curve.

4.4.2. Strontium Isotopic Stratigraphy

The strontium measurements at 3.51, 4 and 4.51 mbsf (green, purple and orange lines in Fig. 11) with uncertainties ranging from 50 to 150 kyr, give ages of 1.36, 1.46 and 1.74 Ma, respectively. A sedimentation rate about 0.26 cm.kyr^{-1} can be estimated at 4.51 mbsf.

Figure 12 combines the estimated ages from oxygen and strontium measurements. The x-axis is the age in millions of years, and on the y-axis is the depth below the seafloor in meters.

The $\delta^{18}\text{O}$ points (corresponding to the ages of the red lines in Fig. 11) line up along a straight axis and have very little dispersion (power regression, $R^2=0.98$). Conversely, the strontium points are more scattered (power regression, $R^2=0.71$). The sediment fraction chosen evolved according to the results obtained during the measurement of the sample series (Table 4). The points outside the grey area were not selected for the age model determination (discussed in section 5.3.2).

The power regression equation gives an age of 4.08 Ma at 11.45 mbsf. Nevertheless, the strontium ages dispersion and uncertainties related to SIS method (up to 1 Ma) do not allow to affirm this result.

5. DISCUSSION

5.1. Foraminiferal sand accumulation in contourite system

5.1.1. Atypical sedimentary facies

The absence of erosional structures, clear bioturbation traces, and the homogeneity of the sedimentary facies observed in MOZ3-CS07 are characteristic and diverge from the current model of organization and classification of contourite sequences proposed by Stow and Faugères (2008). Composed of 70% foraminiferal sand, the sedimentary facies of MOZ3-CS07 is atypical for a homogenous deposit of several meters in thickness on a present-day contourite system. Contourite facies with a similar content of foraminifers are documented from outcrops (Schiller et al., 1994; Carter, 2007; Hüneke et al., 2021) or correspond to sequences of a few tens of centimeters with a lower proportion of foraminifers (e.g., Viana et al., 1998; Brackenridge et al., 2018; de Castro et al., 2020; Hüneke et al., 2020).

In addition to its particular facies, core MOZ3-CS07 presents an extremely low sedimentation rate of about 0.26 cm.kyr^{-1} for the first 4.51 mbsf, corresponding to the lowest sedimentation rates measured on a contourite deposit. This condensed sedimentation appears to be continuous over 11.45 meters and could provide one of the few contourite sedimentary records that allow accessing climate

changes and its regional oceanographic impacts at the Plio-Quaternary scale. Nevertheless, the establishment of such a particular facies and its preservation over time raise some questions, which are discussed in the following sections.

5.1.2. Sedimentary processes inducing foraminiferal sandy contourite formation

The sediments of core MOZ3-CS07 correspond to coarse sand, composed of 70% foraminifer tests and 30% clayey-silty mud. This high content of foraminifer tests is likely due to: (1) a depositional environment with low terrigenous inputs attested by the low sedimentation rates and the pelagic origin of the particles; (2) significant bottom currents inducing the winnowing of fine particles shown by the grain-size results. This last point is supported by the presence of an erosional surface just above the core MOZ3-CS07 (Fig. 2B) indicating that the core is close to an area subject to strong bottom current influence. In these depositional conditions, the low content of fine particles results from their trapping in the interstices between foraminifer tests (Fig. 13). The sedimentation process can be divided into two steps: (1) the pelagic sedimentation, settling of foraminifer tests on the seafloor; (2) the interstitial sedimentation, when suspended particles are trapped in the interstices formed between tests (Fig. 13). This interpretation is supported by the gap observed in the grain-size distribution (Fig. 6) that corresponds to a natural break in the distribution of grain-size fractions that reflects a change of the sediment origin/processes (Smalley, 1966; Pettijohn, 1975). In this foraminiferal sandy contourite, the break separates biogenic (pelagic sedimentation) from terrigenous (interstitial sedimentation) sediments.

For the facies variations, observed along core MOZ3-CS07 (Figs. 4 and 5), it is assumed that:

-for very fine mottled sand, bottom currents are weaker, all the sizes of foraminifer tests can be deposited, increasing the potential of trapping fine particles.

-for foraminiferal pocket, bottom currents are stronger, only larger sized foraminifer tests are deposited. Under these conditions, the surface sediments are reworked, transport of foraminifer tests by saltation/traction allows to resuspend both the fine particles trapped and the small and medium-sized foraminifer tests (corresponds to tests <300 μm). Being transported on the seafloor, the tests are fragmented and concentrated, forming foraminiferal pockets.

One centimeter of deposition in core MOZ3-CS07 records about four thousand years of sedimentation. We assume that the preservation of fine particles (clays and silts) over such a long period results from stable hydrodynamic conditions over the time (more explanations in section 5.3.1) and it seems that once fine particles are trapped in interstices between foraminifer tests, the bottom currents are not strong enough to winnow them except in the case of the foraminiferal pockets.

This foraminiferal contourite facies does not show typical contourite sedimentary layers organized in bi-graded sequences (Gonthier et al., 1984). The only evidence for variations in bottom current speed is the variations in geochemical and grain-size proxies ($\ln(Zr/Rb)$ and sorting/skewness). The two main diagnostic criteria for distinguishing contourite are based on the presence and abundance of bioturbation (e.g., Lovell and Stow, 1981; Gonthier et al., 1984; Wetzel et al., 2008) or on the presence of primary sedimentary structures (e.g., Shanmugan, 2000; Martín-Chivelet et al., 2008). The foraminiferal sandy contourite facies of core MOZ3-CS07 is interpreted slightly bioturbated because of the absence of sedimentary structures. Nevertheless, even on X-ray images, no clear bioturbation structures have been observed. This observation could be explained by a benthic community mainly composed of grazing animals that destroy pre-existing sedimentary structures and do not produce burrows as commonly observed in contourite deposits (summarized in Rodríguez-Tovar et al., 2022).

5.1.3. Estimation of bottom current speed

The equation of McCave et al. (2017) on the value of the "Sortable Silt mean size" (\overline{SS} , corresponds to the grain-size average of the classes between 10 and 63 μm) is applied on the bulk sediment to estimate the current speed according to the following equation: $\overline{SS}=0.808U+15.46$ (with U: the current speed in $\text{cm}\cdot\text{s}^{-1}$). Taking $\overline{SS}=28.63 \mu\text{m}$ (corresponds to the average \overline{SS} of MOZ3-CS07), we obtain $U=16.30 \text{ cm}\cdot\text{s}^{-1}$. Without carbonate dissolution and deflocculating agent, this value is only an estimation of the average current speed (certainly overestimated due to the flocculation process of the finest particles). Nevertheless, the latest work by Miramontes et al. (2021), using the Regional Ocean Modelling System (ROMS, CROCO version: <https://www.croco-ocean.org/>), shows a similar bottom current speeds at the location of the contourite drift where the core MOZ3-CS07 was collected.

Taking the smallest value of \overline{SS} (19.27 μm at 7.29 mbsf), a speed of 4.72 $\text{cm}\cdot\text{s}^{-1}$ is obtained. The maximum current speed is not calculable because in this case no sediment smaller than 63 μm is deposited (at 0.84 mbsf). According to the work of Lonsdale et al. (1972), foraminiferal sand motion threshold is at 17 $\text{cm}\cdot\text{s}^{-1}$. Miller and Komar (1977) and McCave and Hall (2006), also calculated the critical speed for the movement of foraminifers with sizes between 200 and 300 μm and found 20-25 $\text{cm}\cdot\text{s}^{-1}$. Following these estimations, sediments of core MOZ3-CS07 seem to have been deposited under the action of a bottom current speed ranging from 4.72 to 17-20 $\text{cm}\cdot\text{s}^{-1}$.

5.2. Contourite system of the Mozambique Ridge

The results of Babonneau et al. (2022) suggest that the entire contourite system is almost disconnected from continental inputs, fed by hemipelagic/pelagic sediments and sediment transfer processes within the contourite channels. This contourite depositional system provides a perfect study area to investigate contourite without the impact of gravity-driven processes.

5.2.1. Evolution of the sedimentary processes from the channel to the drift

Three major sedimentary sources are identified in figure 10, according to the grain-size modes: (1) suspended particles forming the clayey and fine silty modes composed of clay and mica; (2) biogenic inputs, mainly foraminifer tests forming the coarse sand mode and (3) the along-slope transfer of siliciclastic material (i.e., quartz and feldspars) into the channel creating the fine sand mode. Depending on the location in the contourite system, these sedimentary sources are found in different proportions in the sediment and reflect changes in bottom currents speed creating unimodal or bimodal grain-size distributions. These distributions (Fig. 10) can be divided into two contourite sedimentary processes proposed by Miramontes et al. (2021): (1) contourites dominated by depositional processes and; (2) contourites dominated by winnowing/reworking processes. For each sedimentary process, two sedimentological poles are defined from the cross-plot of “sorting versus D_{50} ” (Fig. 9).

Contourites dominated by depositional processes show a bimodal grain-size distribution developed under weak bottom currents allowing the deposition of fine and coarse particles. For the “mainly terrigenous” pole, corresponding to sediments close to the channel, fine particles are composed of clay and micas, and; coarse particles are composed of quartz and feldspars. For the “mainly biogenic”

pole, corresponding to sediments from the drift, fine particles consist of clay and micas, and coarse particles are composed of foraminifer tests and in lesser proportion of quartz and feldspars.

Contourites dominated by winnowing/reworking processes show an unimodal grain-size distribution, which is set up under strong bottom currents where fine particles are winnowed, and only coarse particles can be deposited. For the “siliciclastic sand” pole, corresponding to sediments close to the channel, coarse particles are composed of quartz and feldspar. For the “foraminiferal sand” pole, corresponding to sediments from the drift, the coarse particles are composed of foraminifer tests.

If the bottom current speed increases, contourites dominated by depositional processes will evolve into contourites dominated by winnowing/reworking processes adopting a siliciclastic or foraminiferal sand depending on the location in the system and thus the composition of the sediment (Fig. 9 and 10).

5.2.2. Contourite endmembers and their relationships

Sorting and size of contourite sediments are controlled by the bottom current speed and sediment sources. Using cross-plots of "sorting versus D_{50} " provide a better characterization of these deposits (Brackenridge et al., 2018; de Castro et al., 2020, 2021a, 2021b; Bankole et al., 2021; Rodrigues et al., 2022). Nevertheless, the continuity and the possible interplay between contourite, hemipelagite and turbidite processes, make it difficult to distinguish clearly these deposits from this type of graph.

The contourite system studied here is disconnected from gravity driven continental inputs, thus only two types of sedimentary deposits are present in this system, contourites and hemipelagites. Based on our results (Fig. 9) and on previous studies (Brackenridge et al., 2018; de Castro et al., 2020, 2021a, 2021b; Bankole et al., 2021) using cross-plots of "sorting versus D_{50} ", two contourite trends can be defined: (1) siliciclastic trend (already shown by de Castro et al., 2021), mainly represented by the sediments of core MOZ3-CS03 and partly by those of MOZ3-CS02; (2) foraminiferal trend, mainly represented by the sediments of core MOZ3-CS07 and partly by those of CS02. Both trends illustrate an increase in current speed from contourites dominated by depositional processes to contourites dominated by winnowing/reworking processes. As foraminifer tests have a lower density than

siliciclastic particles (i.e., quartz), for the same given current speed, they will therefore be larger than siliciclastic particles, thus explaining the size difference between a foraminiferal sand and a siliciclastic sand. These results conducted us to propose the “Contourite Graphical Chart” (inspired by the work of Bankole et al., 2021) allowing to locate and understand the repartition of contourite deposits and their related trends (Fig. 14).

The “Contourite Graphical Chart” highlights three contourite endmembers; the silty contourites, the siliciclastic sandy contourite and the foraminiferal contourite. The silty contourites represent a starting point from which the sedimentary facies will evolve during deposition to another type of contourite facies depending on the current speed and/or the source of sediments. As previously shown by Bankole et al. (2021), silty contourites become hemipelagites in the case where the current speed is almost nil.

Each endmember is associated to a sedimentary process; the silty contourites are associated to depositional processes under low bottom current speed, the sandy siliciclastic and foraminiferal contourites to winnowing or reworking processes (Fig. 14). During deposition or over the time, a siliciclastic sandy contourite can evolve into a foraminiferal contourite if terrigenous inputs decrease or if its distance from the contourite channel increases, as previously shown core MOZ3-CS02 (Fig. 9).

5.3. Bottom current processes and paleoceanographic record

5.3.1. Contourite system in AAIW/NADW interface

The contourite system studied is currently at the depth of the AAIW/NADW interface (Thiéblemont et al., 2019; Babonneau et al., 2022). The processes operating at water mass interfaces in the Mozambique Channel are described by Thiéblemont et al., (2019). Among them, internal waves are suggested by some authors as a relevant mechanism in the erosion and non-deposition of sediments in some contourite systems (e.g., MC/AAIW interface at 800 mbsl; Thiéblemont et al., 2019). The AAIW/NADW interface corresponds to a progressive transition zone where no high value in buoyancy (Brunt-Väisälä) frequency is observed (Thiéblemont et al., 2019), and thus there is probably no intensification of internal wave activity compared to the surrounding water masses.

The study area is on the main pathway of oceanic eddies (Fig. 1). In the Mozambique channel, eddies can affect the whole water column impacting the seafloor in the whole basin (de Ruijter et al., 2002). Schouten et al. (2003) showed that eddies current speed at 2000 mbsl can reach up to 10 cm.s⁻¹. As previously demonstrated by Thiéblemont et al. (2019) and Miramontes et al. (2021), elongated-mounded drifts in the Mozambique Channel at the AAIW and NADW depths are formed by water mass channeling processes under the influence of Coriolis force creating erosive surfaces on the left sides of the channels. These processes would explain erosion surfaces on the eastern flanks of the contourite system (Fig. 2 and 15). Small erosional surfaces on some western flanks of the contourite system could indicate southward flowing of the bottom current due to interactions with the bathymetry forming an anti-clockwise circular current also observed in the modelled bottom current by ROMS (CROCO version, Miramontes et al., 2021). Babonneau et al. (2022) proposed that this circular current around the contourite drift could facilitate the capture of other circular hydrodynamic processes, such as eddies (Fig. 15).

The variability of bottom current speed in the channels (cores MOZ3-CS03 and MOZ3-CS02) is high, allowing both silty-clayey and siliciclastic sediments to be deposited during certain glacial stages, in contrast to the variability of bottom current speed in core MOZ3-CS07, which is much lower and allows the formation of a continuous foraminiferal sandy contourite facies without erosional surfaces indicating relative stable hydrodynamic conditions over time. This difference in bottom current variability between the drift and the channels could be explained by the thickness of the AAIW/NADW interface (~700 m) offering stable conditions even with the Quaternary eustatic variations. The sedimentary variability observed in the western channel (Fig. 3 and 15) could be related to channeling processes that accentuate bottom current speed variations through climate cycles. These variations are also recorded in core MOZ3-CS07 facies and discuss in the following part.

5.3.2. Paleoceanographic record during 100 kyr Quaternary climate cycles

The end of the MPT is observed at 1.55 msbf on core MOZ3-CS07 corresponding to 632ka (Fig. 11). After the MPT, sedimentation rates of 100 kyr climate cycles are calculated from the correlations with the reference curve LR04 (red lines in Fig. 11). The interglacial stages show a higher sedimentation

than the glacial stages with an average rate of 0.5 cm.kyr^{-1} compared to 0.15 cm.kyr^{-1} . The $\ln(\text{Zr/Rb})$ curve reveals a greater intensity of bottom currents during glacial stages than during interglacial stages. The work of Babonneau et al. (2022) has allowed us to propose a general circulation pattern at the scale of the contourite system during the Quaternary period. By combining these results with those of this study, it is possible to propose an interpretation of the dynamics of the AAIW/NADW interface during the 100 kyr climate cycles (Fig. 15):

-interglacial stages: bottom current speed is relatively low (compared to glacial stages). Sandy particles are transported through the western channel, bottom current induce winnowing of fine particles which are deposited by hemipelagic sedimentation on site MOZ3-CS03 and CS02. On the drift, only foraminiferal sands are deposited, between which particles in suspension are trapped.

-glacial stages: bottom current speed is higher. Fine particles continue to be deposited on site MOZ3-CS03 and MOZ3-CS02, but in smaller proportions. For some glacial stages, cores MOZ3-CS03 and MOZ3-CS02 show siliciclastic sands that reflect higher intensity of bottom currents and greater transport (Figs. 3 and 15). On the western side of the drift, coarse foraminifer tests continue to be deposited and are sometimes winnowed and condensed into foraminiferal pockets.

Variations of bottom current speed generated at the AAIW/NADW interface during 100 kyr climate cycles result from the variations of intensity of the AAIW, NADW, the impact of internal waves, eddies and how all these factors are increased or reduced by interaction with the seafloor morphology. As the contourite system is close to the upper part of the NADW, it is assumed that the intensity of the AAIW/NADW interface at this depth depends more on the behavior of the NADW than that of the AAIW.

Molyneux et al. (2007) showed an increase in the influence of the NADW on the Agulhas Plateau (Fig. 1) during glacial periods over the last 200 kyr. Our results confirm that this behavior of the NADW during climatic cycles is the same over the last 633 kyr. The recent study of van der Lubbe et al. (2021) provides a 7 Myr record of wind-driven circulation of the tropical Indian Ocean, as recorded in Mozambique Channel Throughflow (MCT) flow speed variations at the IODP Site U1476 located on the Davie Ridge at 2166 mbsf (Fig. 1). Their results show an increase in MCT flow speed during glacial periods. Coupled with our study, it appears that from the Agulhas Plateau (southern entrance of the

Mozambique Channel) to the Davie Ridge (northern entrance of Mozambique channel), the behavior of the surface and bottom ocean circulation is synchronous in this region over the 100 kyr climatic cycles.

The absence of the MIS 14 on the $\delta^{18}\text{O}$ curves of MOZ3-CS07 and MOZ3-CS03 (Fig. 11), could be linked to the lower sedimentation rates in glacial stages. This isotopic stage corresponds to a short and moderately cold glacial stage, attenuated on the reference curve LR04. The sampling resolution and the condensation of the sedimentary records (especially for MOZ3-CS07) probably contribute to hide this glacial period in the $\delta^{18}\text{O}$ curve of MOZ3-CS07.

4.08 Ma age is estimated at 11.45 m in core MOZ3-CS07 from the power regression on Sr-isotope measurements inside the grey area in figure 12. The points outside the grey area were not selected for the age estimation. These different choices are discussed below.

Measurements of series 1 and 2 were made on bulk sediment. Despite the presence of clay, the values appear consistent except for two samples (at 5 and 8.45 mbsf). These two points outside the grey zone with abnormally old ages (or low strontium ratios) can more likely be explained either by contamination via volcanic ash or by old carbonates from sedimentary structures outside the contourite system, than by a protocol or analytical errors during the analyses.

Measurements of series 3, 4 and 5 are performed on the fraction $>250\ \mu\text{m}$ of the same samples but the samples of series 4 were placed in ultrasonic bath treated with ultrasounds. It would appear that the ultrasound waves destabilize the structure of clay (residual clays probably present within the foraminiferal tests), which are therefore more easily dissolved during the acidic passages and can influence the measured $87\text{Sr}/86\text{Sr}$ ratio (by increasing it because the measured Sr will be the result of both Sr from the detrital fraction which are very radiogenic and Sr from the carbonates).

Despite these precautions, the uncertainties related to the SIS method do not allow confirming an age of 4.08 Ma at the base of core MOZ3-CS07. This age requires verification with other dating methods. Nevertheless, this estimation and the singularity of the foraminiferal sandy

contourite facies of core MOZ3-CS07 highlight its potential as long-term palaeoceanographic record.

6. CONCLUSIONS

This study provides the characterization of a foraminiferal sandy contourite facies from the drift of a contourite system localized in the Limpopo Corridor. This foraminiferal sandy contourite facies diverges from the conceptual contourite facies model and, due to its condensed sedimentation, offers a long-term, low-resolution paleoceanographic record. The comparisons with others contourite facies from the near-by channels allow to understand bottom current processes and variations in sediment distribution through 100 kyr climate cycles in a contourite system with low terrigenous inputs and influenced by the AAIW/NADW interface.

Core MOZ3-CS07 shows continuous and homogenous foraminiferal sandy facies over 11.45 m. This sedimentary facies results from the trapping of fine particles in suspension between the foraminifer tests interstices. This process of interstitial sedimentation induces the deposition of a significant content of clay and silt (about 20%) under stable and intense hydrodynamic conditions over a long period of time with an average sedimentation rate of 0.26 cm.kyr⁻¹.

The cross-plot of "sorting versus D₅₀" allows us to propose the concept of "Graphical Contourite Facies Chart" that helps to characterize the contourite facies and their related sedimentary processes. Three contourite endmembers are identified; silty contourite, siliciclastic sandy contourite and foraminiferal sandy contourite. The silty contourites are considered as a starting point from which the facies can evolve to another endmember depending on the bottom current speed and the nature of the sediment inputs.

At the scale of 100 kyr climate cycles, the contourite system is under the influence of the AAIW/NADW interface. The sedimentation rates are lower and bottom current speed is higher during glacial stages than interglacial stages. These hydrodynamic variations are not visible on the sedimentary facies of core MOZ3-CS07 unlike those of cores located in the near-by channels of the contourite system (MOZ3-CS03 and CS02). These results show that the sediments from the top of the drift (core MOZ3-

CS07) are deposited under relatively stable hydrodynamic conditions compared to those from the channels.

Foraminiferal sandy contourite facies have great potential as sedimentary record. From this study, it appears that contourite systems disconnected from gravity flows provide more easily exploitable and interpretable sedimentary records. Following this reasoning, the depleted continental margins should host areas more favorable for the study of long paleoceanographic record from contourite systems.

7. ACKNOWLEDGMENTS

The PAMELA project (PAssive Margin Exploration Laboratories) is a scientific project led by Ifremer and TotalEnergies in collaboration with Université de Bretagne Occidentale, Université de Rennes 1, Université P&M Curie, CNRS and IFPEN. The authors thank the Captain and the crew of the PAMELA-MOZ03 survey onboard the R/V « Pourquoi pas? ». We also would like to thank Pr. Francisco Javier Hernández-Molina, for his constructive comments that helped us improve the manuscript. We thank the editor Michele Rebesco, the reviewer Antje Voelker and anonymous reviewers for their positive comments which helped us to improve the manuscript.

8. CONFLICT OF INTEREST

We declare that we have no commercial or associative aim that might represent a conflict of interest in connection with the work submitted.

9. DATA AVAILABILITY

Lopes, Ugo; Babonneau, Nathalie; Fierens, Ruth; Révillon, Sidonie; Raison, Francois; Miramontes Elda; Rabineau, Marina; Moulin Maryline; Aslanian, Daniel (submitted), "Foraminiferal sandy contourite of the Mozambique Channel: facies characterization and Paleoceanographic record", Mendeley Data, doi: ...

<https://doi.org/10.21203/rs.3.rs-1111111/v1>

10. REFERENCES

- Babonneau, N., Raison, F., Genêt, A., Lopes, U., Fierens, R., Miramontes, E., ... & Aslanian, D. (2022).** Contourite on the Limpopo Corridor, Mozambique margin: Long-term evolution, facies distribution and Plio-Quaternary processes. *Sedimentology*.
<https://doi.org/10.1111/sed.13045>
- Bankole, S., Stow, D., Smillie, Z., Buckman, J., & Lever, H. (2021).** Mudrock Microstructure: A Technique for Distinguishing between Deep-Water Fine-Grained Sediments. *Minerals*, 11(6), 653. <https://doi.org/10.3390/min11060653>
- Blott, S. J., & Pye, K. (2001).** Gradistat: A grain size distribution and statistics package for the analysis of unconsolidated sediments. *Earth Surface Processes and Landforms*, 1248, 1237–1248
- Brackenridge, R., Stow, D. A. V. & Hernández-Molina, F. J. (2011)** Contourites within a deep-water sequence stratigraphic framework. *Geo-Mar Lett* 31, 343–360.
<https://doi.org/10.1007/s00367-011-0256-9>
- Brackenridge, R. E., Stow, D. A. V., Hernández-Molina, F. J., Jones, C., Mena, A., Alejos, I., Ducassou, E., Llave, E., Ercilla, G., Nombelas, M. A., Perez-Arlucas, M., & Frances, G. (2018).** Textural characteristics and facies of sand-rich contourite depositional systems. *Sedimentology*, 65, 2223–2252. <https://doi.org/10.1111/sed.12463>
- Breitzke, M., Wiles, E., Krockner, R., Watkeys, M. K., & Jokat, W. (2017).** Seafloor morphology in the Mozambique Channel: evidence for long-term persistent bottom-current flow and deep-reaching eddy activity. *Marine Geophysical Research*, 38(3), 241-269.
- Carter, R. M. (2007).** The role of intermediate-depth currents in continental shelf-slope accretion: Canterbury Drifts, SW Pacific Ocean. *Geological Society, London, Special Publications*, 276(1), 129-154. <https://doi.org/10.1144/GSL.SP.2007.276.01.07>
- Counts, J. W., Jorry, S. J., Leroux, E., Miramontes, E., & Jouet, G. (2018).** Sedimentation adjacent to atolls and volcano-cored carbonate platforms in the Mozambique Channel (SW Indian Ocean). *Marine Geology*, 404, 41-59. <https://doi.org/10.1016/j.margeo.2018.07.003>.

- de Castro, S., Hernández-Molina, F. J., Rodríguez-Tovar, F. J., Llave, E., Ng, Z. L., Nishida, N., & Mena, A.** (2020). Contourites and bottom current reworked sands: Bed facies model and implications. *Marine Geology*, 428(January). <https://doi.org/10.1016/j.margeo.2020.106267>
- de Castro, S., Hernández-Molina, F. J., Weger, W., Jiménez-Espejo, F. J., Rodríguez-Tovar, F. J., Mena, A., Llave, E., & Sierro, F. J.** (2021a). Contourite characterization and its discrimination from other deep-water deposits in the Gulf of Cadiz contourite depositional system. *Sedimentology*, 68(3), 987–1027. <https://doi.org/10.1111/sed.12813>
- de Castro, S., Miramontes, E., Dorador, J., Jouet, G., Cattaneo, A., Rodríguez-Tovar, F. J., & Hernández-Molina, F. J.** (2021b). Siliciclastic and bioclastic contouritic sands: Textural and geochemical characterisation. *Marine and Petroleum Geology*, 128(December 2020), 105002. <https://doi.org/10.1016/j.marpetgeo.2021.105002>
- de Ruijter, W. D., Biastoch, A., Drijfhout, S. S., Lutjeharms, J. R. E., Matano, R. P., Pichevin, T., ... & Weijer, W.** (1999). Indian-Atlantic interocean exchange: Dynamics, estimation and impact. *Journal of Geophysical Research: Oceans*, 104(C9), 20885-20910. <https://doi.org/10.1029/1998JC900099>
- de Ruijter, W. P. M., Ridderinkhof, H., Lutjeharms, J. R. E., Schouten, M. W., & Veth, C.** (2002). Observations of the flow in the Mozambique Channel. *Geophysical Research Letters*, 29(10), 3–5. <https://doi.org/10.1029/2001GL013714>
- Elderfield, H.** (1986). Strontium isotope stratigraphy. *Palaeogeography, palaeoclimatology, palaeoecology*, 57(1), 71-90. [https://doi.org/10.1016/0031-0182\(86\)90007-6](https://doi.org/10.1016/0031-0182(86)90007-6)
- Evain, M., Schnürle, P., Leprêtre, A., Verrier, F., Watremez, L., Thompson, J. O. ... & Moulin, M.** (2021). Crustal structure of the East African Limpopo margin, a strike-slip rifted corridor along the continental Mozambique Coastal Plain and North Natal Valley. *Solid Earth*, 12(8), 1865-1897. <https://doi.org/10.5194/se-12-1865-2021>
- Folk, R. L., & Ward, W. C.** (1957). Brazos River Bar: A study in the significance of grain size parameters. *Journal of Sedimentary Petrology*, 27(1), 3–26. <https://doi.org/10.1306/74D70646-2B21-11D7-8648000102C1865D>

- Fonnesu, M., Palermo, D., Galbiati, M., Marchesini, M., Bonamini, E., & Bendias, D.** (2020). A new world-class deep-water play-type, deposited by the syndepositional interaction of turbidity flows and bottom currents: The giant Eocene Coral Field in northern Mozambique. *Marine and Petroleum Geology*, 111(May 2019), 179–201. <https://doi.org/10.1016/j.marpetgeo.2019.07.047>
- Friedman, G. M., & Sanders, J. E.** (1978). *Principals of Sedimentology* (Vol. 50, Issue Chapter 8). <https://doi.org/10.1002/esp.3290040317>
- Gao, Y., Stow, D. A. V., Tang, Y., Xie, X., & Piper, D. J. W.** (2020). Seismic stratigraphy and deep-water sedimentary evolution of the southern Mozambique margin: Central Terrace and Mozambique Fracture Zone. *Marine Geology*, 427(December 2019), 106187. <https://doi.org/10.1016/j.margeo.2020.106187>
- Gonthier, E. G., Faugères, J. C., & Stow, D. A. V.** (1984). Contourite facies of the Faro Drift, Gulf of Cadiz. *Geological Society Special Publication*, 15, 275–292. <https://doi.org/10.1144/GSL.SP.1984.015.01.18>
- Gradstein, F. M., Ogg, J. G., Schmitz, M. B., & Ogg, G. M. (Eds.)**. (2012). *The geologic time scale 2012*. Elsevier.
- Gruetzner, J., Jiménez Espejo, F. J., Lathika, N., Uenzelmann-Neben, G., Hall, I. R., Hemming, S. R., Levay, L. J., Barker, S., Berke, M. A., Brentegani, L., Caley, T., Cartagena-Sierra, A., Charles, C. D., Coenen, J. J., Crespin, J. G., Franzese, A. M., Han, X., Hines, S. K. V., Just, J., ... Zhang, H.** (2019). A New Seismic Stratigraphy in the Indian-Atlantic Ocean Gateway Resembles Major Paleo-Oceanographic Changes of the Last 7 Ma. *Geochemistry, Geophysics, Geosystems*, 20(1), 339–358. <https://doi.org/10.1029/2018GC007668>
- Halo, I., Backeberg, B., Penven, P., Ansorge, I., Reason, C., Ullgren, J.E.** (2014). Eddy properties in the Mozambique Channel: a comparison between observations and two numerical ocean circulation models. *Deep sea Res. II Top. Stud. Oceanogr.* 100, 38–53. <https://doi.org/10.1016/j.dsr2.2013.10.015>

- Hancke, L., Roberts, M. J., & Ternon, J. F.** (2014). Surface drifter trajectories highlight flow pathways in the Mozambique Channel. *Deep Sea Research Part II: Topical Studies in Oceanography*, 100, 27-37. <https://doi.org/10.1016/j.dsr2.2013.10.014>
- Heezen, B. C., & Hollister, C.** (1964). Deep sea current evidence from abyssal sediments. *Marine Geology*, 1(2), 141-174. [https://doi.org/10.1016/0025-3227\(64\)90012-X](https://doi.org/10.1016/0025-3227(64)90012-X)
- Hernández-Molina, J., Llave, E., Somoza, L., Fernández-Puga, M. C., Maestro, A., León, R., ... & Gardner, J.** (2003). Looking for clues to paleoceanographic imprints: a diagnosis of the Gulf of Cadiz contourite depositional systems. *Geology*, 31(1), 19-22. [https://doi.org/10.1130/0091-7613\(2003\)031%3C0019:LFCTPI%3E2.0.CO;2](https://doi.org/10.1130/0091-7613(2003)031%3C0019:LFCTPI%3E2.0.CO;2)
- Hernández-Molina, F. J., Hüneke, H., Rodríguez-Tovar, F. J., Ng, Z. L., Llave, E., Mena, A., ... & de la Vara, A.** (2022). Eocene to middle Miocene contourite deposits in Cyprus: A record of Indian Gateway evolution. *Global and Planetary Change*, 219, 103983. <https://doi.org/10.1016/j.gloplacha.2022.103983>
- Hollister, C.D.**, (1967). Sediment distribution and deep circulation in the western North Atlantic. (PhD thesis) Columbia University, New York.
- Huizhong, W., & McCave, I. N.** (1990). Distinguishing climatic and current effects in mid-Pleistocene sediments of Hatton and Gardar Drifts, NE Atlantic. *Journal of the Geological society*, 147(2), 373-383. <https://doi.org/10.1144/gsjgs.147.2.0373>
- Hüneke, H., Hernández-molina, F. J., Rodríguez-Tovar, F. J., Llave, E., Chiarella, D., Mena, A., & Stow, D. A. V.** (2020). Diagnostic criteria using microfacies for calcareous contourites, turbidites and pelagites in the Eocene - Miocene slope succession, southern Cyprus. *International Association of Sedimentologists*. <https://doi.org/10.1111/sed.12792>
- Hüneke, H., Hernández-Molina, F. J., Rodríguez-Tovar, F. J., Llave, E., Chiarella, D., Mena, A., & Stow, D. A. V.** (2021). Diagnostic criteria using microfacies for calcareous contourites, turbidites and pelagites in the Eocene-Miocene slope succession, southern Cyprus. *Sedimentology*, 68(2), 557-592. <https://doi.org/10.1111/sed.12792>

- Jokat, W., Boebel, T., König, M., & Meyer, U.** (2003). Timing and geometry of early Gondwana breakup. *Journal of Geophysical Research*, 108. <https://doi.org/10.1029/2002JB001802>
- Knutz, P. C.** (2008). Palaeoceanographic significance of contourite drifts. *Developments in sedimentology*, 60, 511-535. [https://doi.org/10.1016/S0070-4571\(08\)10024-3](https://doi.org/10.1016/S0070-4571(08)10024-3)
- Krüger, S., Leuschner, D. C., Ehrmann, W., Schmiedl, G., & Mackensen, A.** (2012). North Atlantic Deep Water and Antarctic Bottom Water variability during the last 200 ka recorded in an abyssal sediment core off South Africa. *Global and Planetary Change*, 80, 180-189. <https://doi.org/10.1016/j.gloplacha.2011.10.001>
- Leinweber, V. T., Klingelhoefer, F., Neben, S., Reichert, C., Aslanian, D., Matias, L. ... & Jokat, W.** (2013). The crustal structure of the Central Mozambique continental margin—Wide-angle seismic, gravity and magnetic study in the Mozambique Channel, Eastern Africa. *Tectonophysics*, 599, 170-196. <https://doi.org/10.1016/j.tecto.2013.04.015>
- Li, H., Tang, Y., Moulin, M., Aslanian, D., Evain, M., Schnurle, P. ... & Li, J.** (2021). Seismic evidence for crustal architecture and stratigraphy of the Limpopo Corridor: New insights into the evolution of the sheared margin offshore southern Mozambique. *Marine Geology*, 435, 106468. <https://doi.org/10.1016/j.margeo.2021.106468>
- Lisiecki, L. E., & Raymo, M. E.** (2005). A Pliocene-Pleistocene stack of 57 globally distributed benthic $\delta^{18}\text{O}$ records. *20(May)*, 1-17. <https://doi.org/https://doi.org/10.1029/2004PA001071>
- Lonsdale, P., Normark, W. R., & Newman, W. A.** (1972). Sedimentation and erosion on Horizon Guyot. *Geological Society of America Bulletin*, 83(2), 289-316. [https://doi.org/10.1130/0016-7606\(1972\)83\[289:SAEOHG\]2.0.CO;2](https://doi.org/10.1130/0016-7606(1972)83[289:SAEOHG]2.0.CO;2)
- Lonsdale, P., Malfait, B.,** (1974). Abyssal dunes of foraminiferal sand on the Carnegie Ridge. *Geol. Soc. Am. Bull.* 85, 1697-1712. [https://doi.org/10.1130/0016-7606\(1974\)85%3C1697:ADOF50%3E2.0.CO;2](https://doi.org/10.1130/0016-7606(1974)85%3C1697:ADOF50%3E2.0.CO;2)
- Lovell, J. P. B., & Stow, D. A. V.** (1981). Identification of ancient sandy contourites. *Geology*, 9(8), 347-349. [https://doi.org/10.1130/0091-7613\(1981\)9<347:IOASC>2.0.CO;2](https://doi.org/10.1130/0091-7613(1981)9<347:IOASC>2.0.CO;2)

- Martín-Chivelet, J., Fregenal-Martínez, M. A., & Chacón, B.** (2008). Traction structures in contourites. *Developments in Sedimentology*, 60, 157-182. [https://doi.org/10.1016/S0070-4571\(08\)10010-3](https://doi.org/10.1016/S0070-4571(08)10010-3)
- Martorelli, E., Bosman, A., Casalbore, D., Chiocci, F., Conte, A. M., di Bella, L., Ercilla, G., Falcini, F., Falco, P., Frezza, V., Gaglianone, G., Giaccio, B., & Mancini, M.** (2021). Mid-to-late Holocene upper slope contourite deposits off Capo Vaticano (Mediterranean Sea): High-resolution record of contourite cyclicity, bottom current variability and sandy facies. *Marine Geology*, 431(November 2020), 106372. <https://doi.org/10.1016/j.margeo.2020.106372>
- Matsinhe, N. D., Tang, Y., Li, C., Li, J., Mahanjane, E. S., Li, H., & Fang, Y.** (2021). The crustal nature of the northern Mozambique Ridge, Southwest Indian Ocean. *Acta Oceanol. Sin*, 40(7), 170–182. <https://doi.org/10.1007/s13131-021-1747-9>
- McArthur, J. M.** (1994). Recent trends in strontium isotope stratigraphy. *Terra nova*, 6(4), 331-358. <https://doi.org/10.1111/j.1365-3121.1994.tb00507.x>
- McArthur, J. M., Howarth, R. J., & Shields, G. A.** (2012). Strontium isotope stratigraphy. In *The Geologic Time Scale 2012*. Felix M. Gradstein, James G. Ogg, Mark Schmitz and Gabi Ogg. <https://doi.org/10.1016/B978-0-444-59425-9.00007-X>
- McCave, I. N., & Hall, I. R.** (2006). Size sorting in marine muds: Processes, pitfalls, and prospects for paleoflow- speed proxies. *Geochemistry*, 7(10). <https://doi.org/10.1029/2006GC001284>
- McCave, I. N., Thornalley, D. J. R., & Hall, I. R.** (2017). Relation of sortable silt grain size to deep sea current speeds: Calibration of the 'Mud Current Meter.' *Deep sea Research Part I: Oceanographic Research Papers*, 127(July), 1–12. <https://doi.org/10.1016/j.dsr.2017.07.003>
- Miller, M. C., & Komar, P. D.** (1977). The development of sediment threshold curves for unusual environments (Mars) and for inadequately studied materials (foram sands). *Sedimentology*, 24, 709–721. <https://doi.org/10.1111/j.1365-3091.1977.tb00266.x>
- Miramontes, E., Cattaneo, A., Jouet, G., Thereau, E., Thomas, Y., Rovere, M., ... & Trincardi, F.** (2016). The Pianosa contourite depositional system (northern Tyrrhenian Sea): Drift morphology and

Plio-Quaternary stratigraphic evolution. *Marine Geology*, 378, 20-42.
<https://doi.org/10.1016/j.margeo.2015.11.004>

Miramontes, E., Garziglia, S., Sultan, N., Jouet, G., & Cattaneo, A. (2018). Morphological control of slope instability in contourites: a geotechnical approach. *Landslides*, 15, 1085-1095.
<https://doi.org/10.1007/s10346-018-0956-6>

Miramontes, E., Penven, P., Fierens, R., Droz, L., Toucanne, S., Jorry, S. J., ... & Raisson, F. (2019). The influence of bottom currents on the Zambezi Valley morphology (Mozambique Channel, SW Indian Ocean): In situ current observations and hydrodynamic modelling. *Marine Geology*, 410, 42-55. <https://doi.org/10.1016/j.margeo.2019.01.002>

Miramontes, E., Jouet, G., Thereau, E., Bruno, M., Penven, P., Guerin, C., ... & Cattaneo, A. (2020). The impact of internal waves on upper continental slopes: insights from the Mozambican margin (southwest Indian Ocean). *Earth Surface Processes and Landforms*, 45(6), 1469-1482.
<https://doi.org/10.1002/esp.4818>

Miramontes, E., Thiéblemont, A., Babonneau, N., Penven, P., Raisson, F., Droz, L., Jorry, S. J., Fierens, R., Counts, J. W., Wilckens, H., Cattaneo, A., & Jouet, G. (2021). Contourite and mixed turbidite-contourite systems in the Mozambique Channel (SW Indian Ocean): Link between geometry, sediment characteristics and modelled bottom currents. *Marine Geology*, 437(May).
<https://doi.org/https://doi.org/10.1016/j.margeo.2021.106502>

Molyneux, E. G., Hall, I. R., Zahn, R., & Diz, P. (2007). Deep water variability on the southern Agulhas Plateau: Interhemispheric links over the past 170 ka. *Paleoceanography*, 22(4).
<https://doi.org/10.1029/2006PA001407>

Mosher, D. C., Campbell, D. C., Gardner, J. v, Piper, D. J. W., Chaytor, J. D., & Rebesco, M. (2017). The role of deep-water sedimentary processes in shaping a continental margin: The Northwest Atlantic. *Marine Geology*, 393(August), 245-259.
<https://doi.org/10.1016/j.margeo.2017.08.018>

Moulin M. and Aslanian D. (2016) PAMELA-MOZ03 cruise, RV Pourquoi pas ?
<http://dx.doi.org/10.17600/16001600>

- Moulin, M., Aslanian, D., Evain, M., Leprêtre, A., Schnurle, P., Verrier, F., ... & PAMELA-MOZ35 Team.** (2020). Gondwana breakup: messages from the North Natal Valley. *Terra Nova*, 32(3), 205-214.
- Past Interglacials Working Group of PAGES.** (2016). Interglacials of the last 800,000 years. *Reviews of Geophysics*, 54(1), 162-219. <https://doi.org/10.1002/2015RG000482>
- Pettijohn, F. J.** (1975). *Sedimentary rocks* (Vol. 3, p. 628). New York: Harper & Row
- Pin, C., & Zalduegui, J. S.** (1997). Sequential separation of light rare-earth elements, thorium and uranium by miniaturized extraction chromatography: application to isotopic analyses of silicate rocks. *Analytica Chimica Acta*, 339(1-2), 79-89. [https://doi.org/10.1016/S0003-2670\(96\)00499-0](https://doi.org/10.1016/S0003-2670(96)00499-0)
- Rebesco, M.** (2005). Contourites. *Encyclopedia of Geology*, 513–527. <https://doi.org/https://doi.org/10.1016/B0-12-369396-9/00497-4>
- Rebesco, M., Camerlenghi, A., & van Loon, A. J.** (2008). Contourite Research. In *Contourites*. [https://doi.org/10.1016/S0070-4571\(08\)10001-2](https://doi.org/10.1016/S0070-4571(08)10001-2)
- Robinson, S. G., & McCave, I. N.** (1994). Orbital forcing of bottom-current enhanced sedimentation on Feni Drift, NE Atlantic, during the mid-Pleistocene. *Paleoceanography*, 9(6), 943-972. <https://doi.org/10.1029/94PA01439>
- Rodrigues, S., Hernández-Molina, F. J., Hillenbrand, C. -D., Lucchi, R. G., Rodríguez-Tovar, F. J., Rebesco, M., & Larter, R. D.** (2022). Recognizing key sedimentary facies and their distribution in mixed turbidite–contourite depositional systems: The case of the Pacific margin of the Antarctic Peninsula. *Sedimentology*. <https://doi.org/10.1111/sed.12978>
- Rodríguez-Tovar, F. J.** (2022). Ichnological analysis: A tool to characterize deep-marine processes and sediments. *Earth-Science Reviews*, 228, 104014. <https://doi.org/10.1016/j.earscirev.2022.104014>
- de Ruijter, W. P., Ridderinkhof, H., Lutjeharms, J. R., Schouten, M. W., & Veth, C.** (2002). Observations of the flow in the Mozambique Channel. *Geophysical Research Letters*, 29(10), 140-1. <https://doi.org/10.1029/2001GL013714>

- Sætre, R., & da Silva, A. J.** (1984). The circulation of the Mozambique Channel. *Deep sea Research*, 31(5), 485–508. [https://doi.org/10.1016/0198-0149\(84\)90098-0](https://doi.org/10.1016/0198-0149(84)90098-0)
- Sansom, P.** (2018). Hybrid turbidite–contourite systems of the Tanzanian margin. *Petroleum Geoscience*, 24(3), 258–276. <https://doi.org/10.1144/petgeo2018-044>
- Schiller, D. M., Seubert, B. W., Musliki, S., & Abdullah, M.** (1994). The reservoir potential of globigerinid sands in Indonesia.
- Schouten, M. W., de Ruijter, W. P. M., van Leuwen, P. J., & Ridderinkhof, H.** (2003). Eddies and variability in the Mozambique Channel. *Deep sea Research II*, 50, 1987–2003. [https://doi.org/10.1016/S0967-0645\(03\)00042-0](https://doi.org/10.1016/S0967-0645(03)00042-0)
- Shanmugam, G.** (2000). 50 years of the turbidite paradigm (1950s—1990s): deep-water processes and facies models—a critical perspective. *Marine and Petroleum Geology*, 17(2), 285–342. [https://doi.org/10.1016/S0264-8172\(99\)00011-2](https://doi.org/10.1016/S0264-8172(99)00011-2)
- Sloyan, B. M., & Rintoul, S. R.** (2001). Circulation, renewal, and modification of Antarctic Mode and Intermediate Water. *Journal of physical oceanography*, 31(4), 1005–1030. [https://doi.org/10.1175/1520-0485\(2001\)031%3C1005:CRAMOA%3E2.0.CO;2](https://doi.org/10.1175/1520-0485(2001)031%3C1005:CRAMOA%3E2.0.CO;2)
- Smalley, I. J.** (1966). Formation of quartz sand. *Nature*, 221, 476–479.
- Stow, D. A. V., Faugères, J.-C., Howe, J. A., Pudsey, C. J., & Viana, A. R.** (2002). Bottom currents, contourites and deep-sea sediment drifts: current state-of-the-art. *The Geological Society of London*, 22, 7–20. <https://doi.org/10.1144/GSL.MEM.2002.022.01.02>
- Stow, D. A. V., & Faugères, J.-C.** (2008). Contourite Facies and the Facies Model. *Developments in Sedimentology*, 60(08), 223–256. [https://doi.org/10.1016/S0070-4571\(08\)10013-9](https://doi.org/10.1016/S0070-4571(08)10013-9)
- Stow, D. A. V., & Smillie, Z.** (2020). Distinguishing between deep-water sediment facies: Turbidites, contourites and hemipelagites. *Geosciences*, 10(2), 68. <https://doi.org/10.3390/geosciences10020068>
- Swart, N. C., Lutjeharms, J. R. E., Ridderinkhof, H., & De Ruijter, W. P. M.** (2010). Observed characteristics of Mozambique Channel eddies. *Journal of Geophysical Research: Oceans*, 115(C9). <https://doi.org/10.1029/2009JC005875>

- Tallobre, C.** (2017). Mise en évidence d'un système de dépôt contouritique et des processus sédimentaires associés sur le plateau de Demerara (marge guyanaise).
- Thiéblemont, A., Hernández-Molina, F. J., Miramontes, E., Raisson, F., & Penven, P.** (2019). Contourite depositional systems along the Mozambique channel: The interplay between bottom currents and sedimentary processes. *Deep sea Research Part I: Oceanographic Research Papers*, 147(February), 79–99. <https://doi.org/10.1016/j.dsr.2019.03.012>
- Thiéblemont, A., Hernández-molina, F. J., Ponte, J., Robin, C., Guillocheau, F., Cazzola, C., & Raisson, F.** (2020). Seismic stratigraphic framework and depositional history for Cretaceous and Cenozoic contourite depositional systems of the Mozambique Channel, SW Indian Ocean. *Marine Geology*, 425(March), 106192. <https://doi.org/10.1016/j.margeo.2020.106192>
- Thompson, J. O., Moulin, M., Aslanian, D., De Clarens, P., & Guillocheau, F.** (2019). New starting point for the Indian Ocean: Second phase of breakup for Gondwana. *Earth-Science Reviews*, 191, 26-56. <https://doi.org/10.1016/j.earscirev.2019.01.018>
- Ullgren, J.E., van Aken, H.M., Ridderinkhof, H., de Ruijter, W.P.M.,** (2012). The hydrography of the Mozambique Channel from six years of continuous temperature, salinity, and speed observations. *Deep sea Res. I Oceanogr. Res. Pap.* 69, 36–50. <https://doi.org/10.1016/j.dsr.2012.07.003>
- van Aken, H. M. van, Ridderinkhof, H., & de Ruijter, W. P. M.** (2004). North Atlantic deep water in the south-western Indian Ocean. 51, 755–776. <https://doi.org/10.1016/j.dsr.2004.01.008>
- van der Lubbe, H. J. L., Hall, I. R., Barker, S., Hemming, S. R., Baars, T. F., Starr, A., ... & Joordens, J. C. A.** (2021). Indo-Pacific Walker circulation drove Pleistocene African aridification. *Nature*, 598(7882), 618-623. <https://doi.org/10.1038/s41586-021-03896-3>
- Vandorpe, T., Collart, T., Cnudde, V., Lebreiro, S., Hernández-Molina, F. J., Alonso, B., Mena, A., Antón, L., & van Rooij, D.** (2019). Quantitative characterisation of contourite deposits using medical CT. *Marine Geology*, 417(November 2018), 106003. <https://doi.org/10.1016/j.margeo.2019.106003>

- Viana, A. R., Faugères, J. C., & Stow, D. A. V.** (1998). Bottom-current-controlled sand deposits—a review of modern shallow-to deep-water environments. *Sedimentary Geology*, 115(1-4), 53-80. [https://doi.org/10.1016/S0037-0738\(97\)00087-0](https://doi.org/10.1016/S0037-0738(97)00087-0)
- Viana, A. R., & Rebesco, M.** (2007). Economic and Palaeoceanographic Significance of Contourite Deposits. <https://doi.org/https://doi.org/10.1144/GSL.SP.2007.276>
- Watkeys, M. K., & Sokoutis, D.** (1998). Transtension in southeastern Africa associated with Gondwana break-up. *Geological Society, London, Special Publications*, 135(1), 203-214. <https://doi.org/10.1144/GSL.SP.1998.135.01.13>
- Wetzel, A., Werner, F., & Stow, D. A. V.** (2008). Bioturbation and biogenic sedimentary structures in contourites. *Developments in sedimentology*, 60, 183-202. [https://doi.org/10.1016/S0070-4571\(08\)10011-5](https://doi.org/10.1016/S0070-4571(08)10011-5)
- Wu, L., Wilson, D. J., Wang, R., Yin, X., Chen, Z., Xiao, W., & Huang, M.** (2020). Evaluating Zr/Rb ratio from XRF scanning as an indicator of grain-size variations of glaciomarine sediments in the Southern Ocean. *Geochemistry, Geophysics, Geosystems*, 21(11), e2020GC009350. <https://doi.org/10.1029/2020GC009350>
- Yu, X., Stow, D. A. V., Smillie, Z., Esentia, I., Brackenridge, R., Xie, X., Bankole, S., Ducassou, E., & Llave, E.** (2020). Contourite porosity, grain size and reservoir characteristics. *Marine and Petroleum Geology*, 117(January), 104392. <https://doi.org/10.1016/j.marpetgeo.2020.104392>

11. LIST OF FIGURES

Figure 1. Bathymetric map of the Mozambique Channel showing the main physiographic domains and ocean circulation. The red rectangle corresponds to the study area. The white circles correspond to the location of the main eddies and their pathway indicate by the white arrow (Hancke et al., 2014).

Figure 2. A) Detailed bathymetric map showing the contourite system morphology and the location of sediment cores. The grey dashed lines correspond to the isobaths. B) Detailed bathymetric map showing the elements of the contourite system studied and the suggested bottom current direction according to the observed erosional surfaces in figure 2C and the modelled bottom currents of the

Regional Ocean Modelling System (ROMS, CROCO version; Miramontes et al., 2021). C) CHIRP profile MOZ3-SDS 0038 across the northern high (Fig. 2A) and location of sediment cores. The solid red lines highlight seismic reflections.

Figure 3. Proposed stratigraphic correlation between the five cores MOZ3-CS03, MOZ3-CS02, MOZ3-CS07, MOZ3-CS06 and MOZ3-CS05 based on the isotopic stratigraphy, X-Ray Fluorescence log-ratio (modified from Babonneau et al., 2022). ^{14}C : radiocarbon dating; SIS: Strontium Isotope Stratigraphy method. Bottom right shows the synthesis of the sedimentary architecture of the contourite system since the Cretaceous (from Babonneau et al., 2022).

Figure 4. Sedimentological facies and characterization of core MOZ3-CS07, including laser grain-size analyses, physical measurements, X-Ray Fluorescence log-ratios and a zoom on potential laminations with X-Ray image (location shown with a red rectangle).

Figure 5. Sedimentological description of the section 3 from core MOZ3-CS07 as example for the entire core. A) X-Ray image, physical measurements, facies, high resolution photo, median grain size and fine particles content (clay + silt). B) Mineral composition at 2.36 mbsf obtained by QEMSCAN ® technology. C) Photo of the fraction $>125\ \mu\text{m}$ at 2.39 mbsf showing a high abundance of foraminifer tests.

Figure 6. Average grain-size distribution of core MOZ3-CS07, associated cumulative frequency curve and thin section photography analyzed by QEMSCAN. Ap: apatite. The grain size at $30\ \mu\text{m}$ is chosen to separate terrigenous from biogenic particles.

Figure 7. Graphs showing the spectral variability for each type of modal grain-size distribution of core MOZ3-CS07. Each graph gathers the distributions of 9 randomly selected samples. $<30\ \mu\text{m}$ correspond to the proportion of the fraction inferior at $30\ \mu\text{m}$.

Figure 8. A) Cross-plot skewness (Φ) versus D_{50} . B) Cross-plot sorting (Φ) versus D_{50} , for all the grain-size analysis of core MOZ3-CS07 according to their modal distributions. Unimodal distributions show a different trend than the others with a sediment more symmetrical and better sorted when the grain size increase.

Figure 9. Interpreted cross-plot sorting (Φ) versus D_{50} , for all the grain-size analysis of cores MOZ3-CS03-CS02-CS07 and CS06 (see location in Fig. 2). Four sedimentological poles are identified, gathered into two distinct trends showing the transition from sediments dominated by depositional processes to sediments dominated by winnowing/reworking processes.

Figure 10. Average grain-size distribution and parameters (Folk and Ward logarithmic method) for each sedimentological pole (Fig. 9), associated their cumulative frequency curves and their interpretation in terms of sedimentary processes, current speed, contourite trends (siliciclastic or foraminiferal) and location in the contourite system. The nature of the modes is based on QEMSCAN analysis. Note that siliciclastic sand and foraminiferal sand grain-size distributions have the same shape but with a shift of the coarsest mode due to the nature of the sediment.

Figure 11. Stratigraphic correlations between the first 5 mbsf of MOZ3-CS07, MOZ3-CS03 and the reference curve LR04 (Lisiecki and Raymo, 2005) using XRF log-ratios (Ca/Fe and Zr/Rb) and $\delta^{18}\text{O}$ measurements. The end of the MPT is estimated at 1.53 mbsf on core MOZ3-CS07 (632 ka). The green, purple and orange lines correspond to strontium isotope measurements and their uncertainties in dashed lines.

Figure 12. Graph gathering estimated ages from correlations of the $\delta^{18}\text{O}$ curve (red lines in Fig. 11) and ages obtained by Sr-Isotope Stratigraphy method for core MOZ3-CS07. The grey area indicates points selected for the power regression. The dashed black line corresponds to the power regression giving an age of 4.08 Ma at the base of the core.

Figure 13. Interpreted sedimentological process at the origin of the foraminiferal sand of core MOZ3-CS07 and its facies variations by interstitial sedimentation.

Figure 14. Concept of “Contourite Graphical Chart” corresponding to the preferential location of contourite deposits in cross-plot sorting (Φ) versus D_{50} and the existing continuity between them (inspired from Bankole et al., 2021). Three contourite endmembers are identified.

Figure 15. Schematic representation of sedimentary processes, bottom current speed variations over 100 kyr climatic cycles in the AAIW/NADW interface and possible impact of deep anti-clockwise

eddies in the contourite system (modified from Babonneau et al., 2022). During interglacial stages, bottom current speed is lower than during glacial stages.

12. LIST OF TABLES

Table 1. List and characteristics of the CALYPSO piston cores collected during the PAMELA-MOZ3 cruise.

Table 2. Summarize of data acquired on the CALYPSO piston cores. In red are the data previously acquired by Babonneau et al. (2022). Res. = Resolution; MSCL = Multi-Sensor Core Logger; XRF = X-Ray Fluorescence; ^{14}C = radiocarbon dating; $\delta^{18}\text{O}$ = O-isotope measurements (*G. ruber*); $^{87}\text{Sr}/^{86}\text{Sr}$ = Sr-isotope measurements.

Table 3. Mineral composition obtained on thin sections by QEMSCAN analysis on core MOZ3-CS07.

Table 4. Summarize of strontium series measurements made on core MOZ3-CS07 presented in figure 12. Sigma (σ) correspond to the standard deviation of the 6th decimal. In red are the data previously acquired by Babonneau et al., (2022).

13. FIGURES

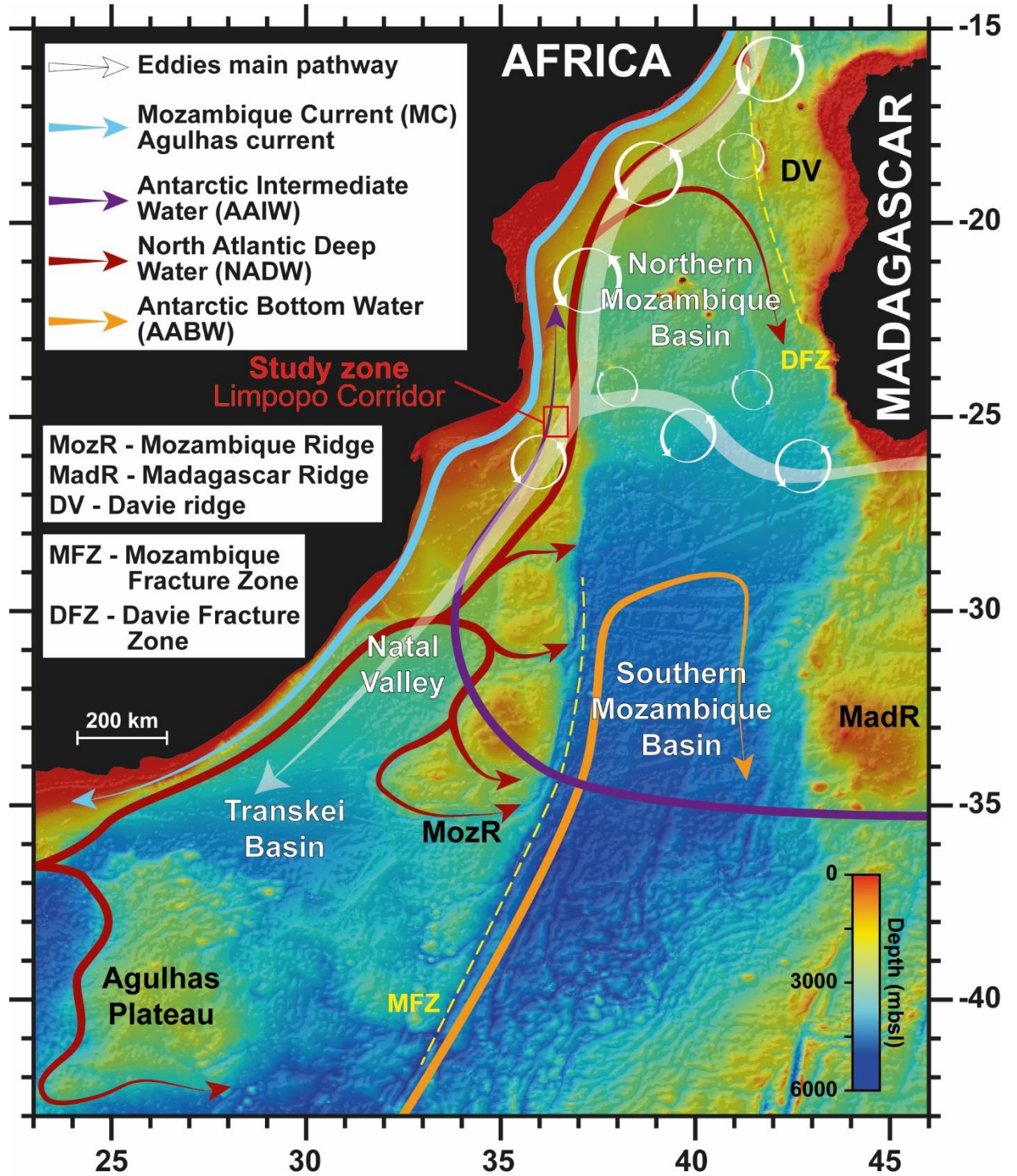


Figure 1. Bathymetric map of the Mozambique Channel showing the main physiographic domains and ocean circulation. The red rectangle corresponds to the study area. The white circles correspond to the location of the main eddies and their pathway indicate by the white arrow (Hancke et al., 2014).

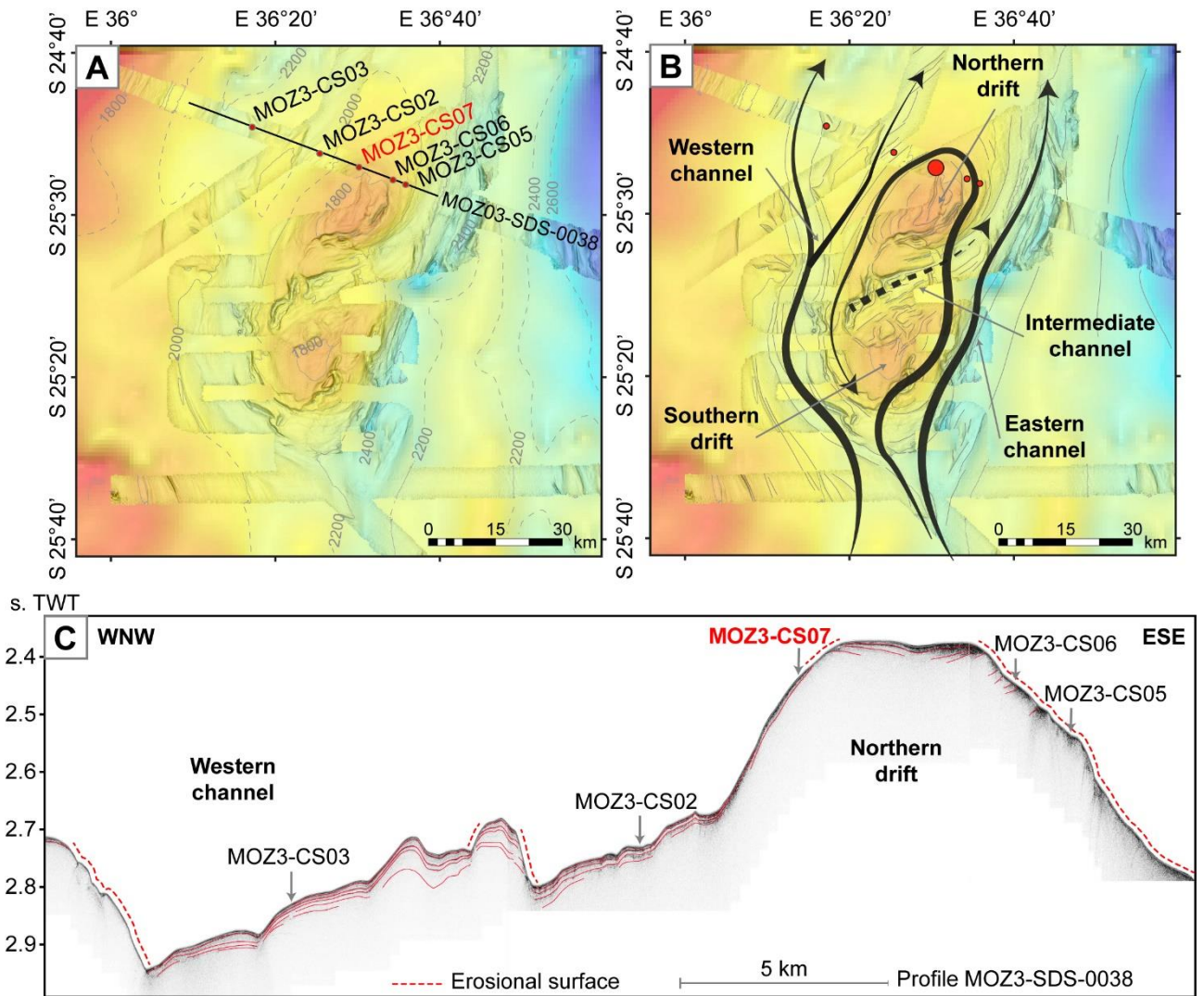


Figure 2. A) Detailed bathymetric map showing the contourite system morphology and the location of sediment cores. The grey dashed lines correspond to the isobaths. B) Detailed bathymetric map showing the elements of the contourite system studied and the suggested bottom current direction according to the observed erosional surfaces in figure 2C and the modelled bottom currents of the Regional Ocean Modelling System (ROMS, CROCO version; Miramontes et al., 2021). C) CHIRP profile MOZ3-SDS 0038 across the northern high (Fig. 2A) and location of sediment cores. The solid red lines highlight seismic reflections.

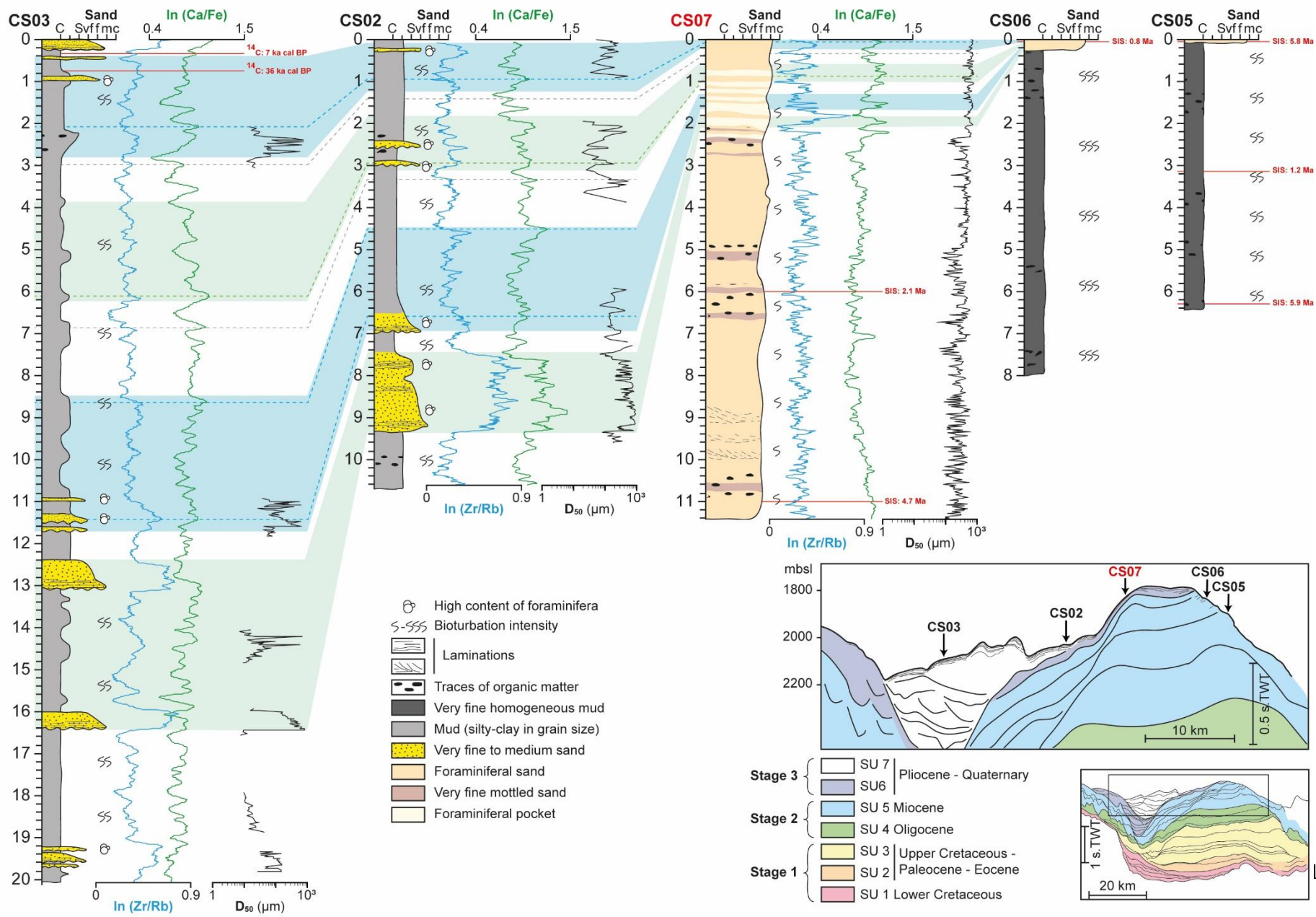


Figure 3. Proposed stratigraphic correlation between the five cores MOZ3-CS03, MOZ3-CS02, MOZ3-CS07, MOZ3-CS06 and MOZ3-CS05 based on the isotopic stratigraphy, X-Ray Fluorescence log-ratio (modified from Babonneau et al., 2022). ¹⁴C: radiocarbon dating; SIS: Strontium Isotope Stratigraphy method. Bottom right shows the synthesis of the sedimentary architecture of the contourite system since the Cretaceous (from Babonneau et al., 2022).

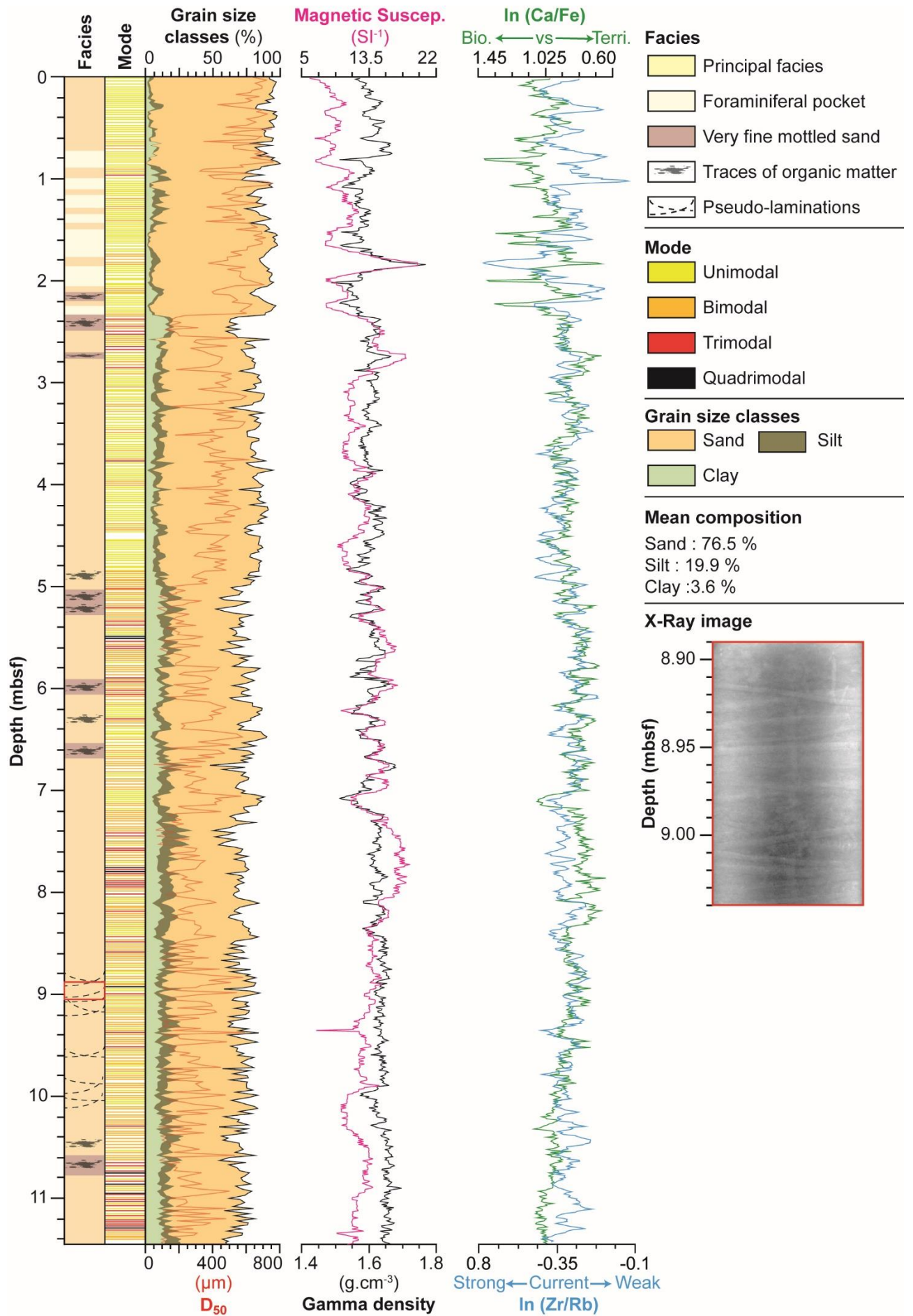


Figure 4. Sedimentological facies and characterization of core MOZ3-CS07, including laser grain-size analyses, physical measurements, X-Ray Fluorescence log-ratios and a zoom on potential laminations with X-Ray image (location shown with a red rectangle).

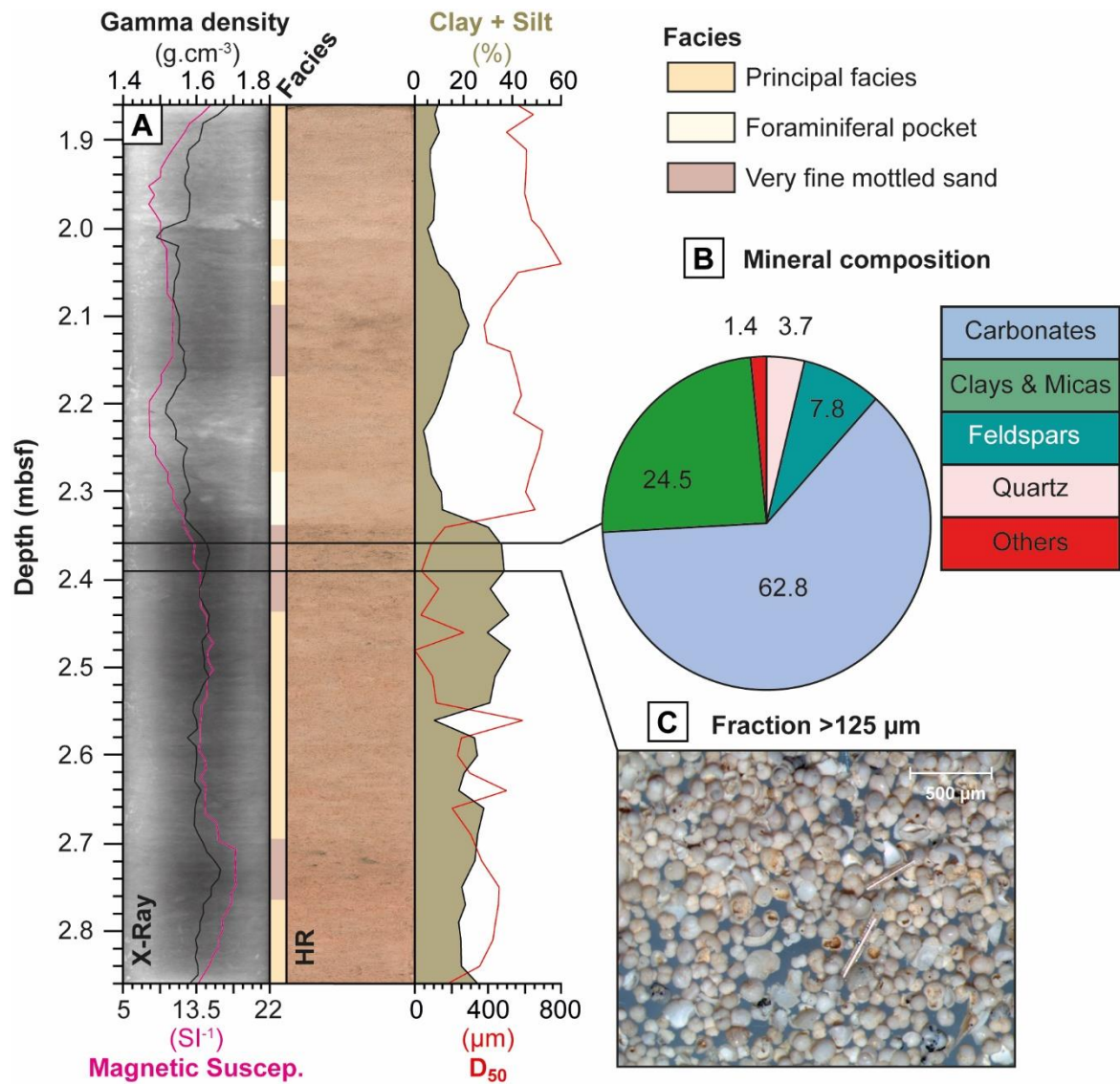


Figure 5. Sedimentological description of the section 3 from core MOZ3-CS07 as example for the entire core. A) X-Ray image, physical measurements, facies, high resolution photo, median grain size and fine particles content (clay + silt). B) Mineral composition at 2.36 mbsf obtained by QEMSCAN ® technology. C) Photo of the fraction >125 μm at 2.39 mbsf showing a high abundance of foraminifer tests.

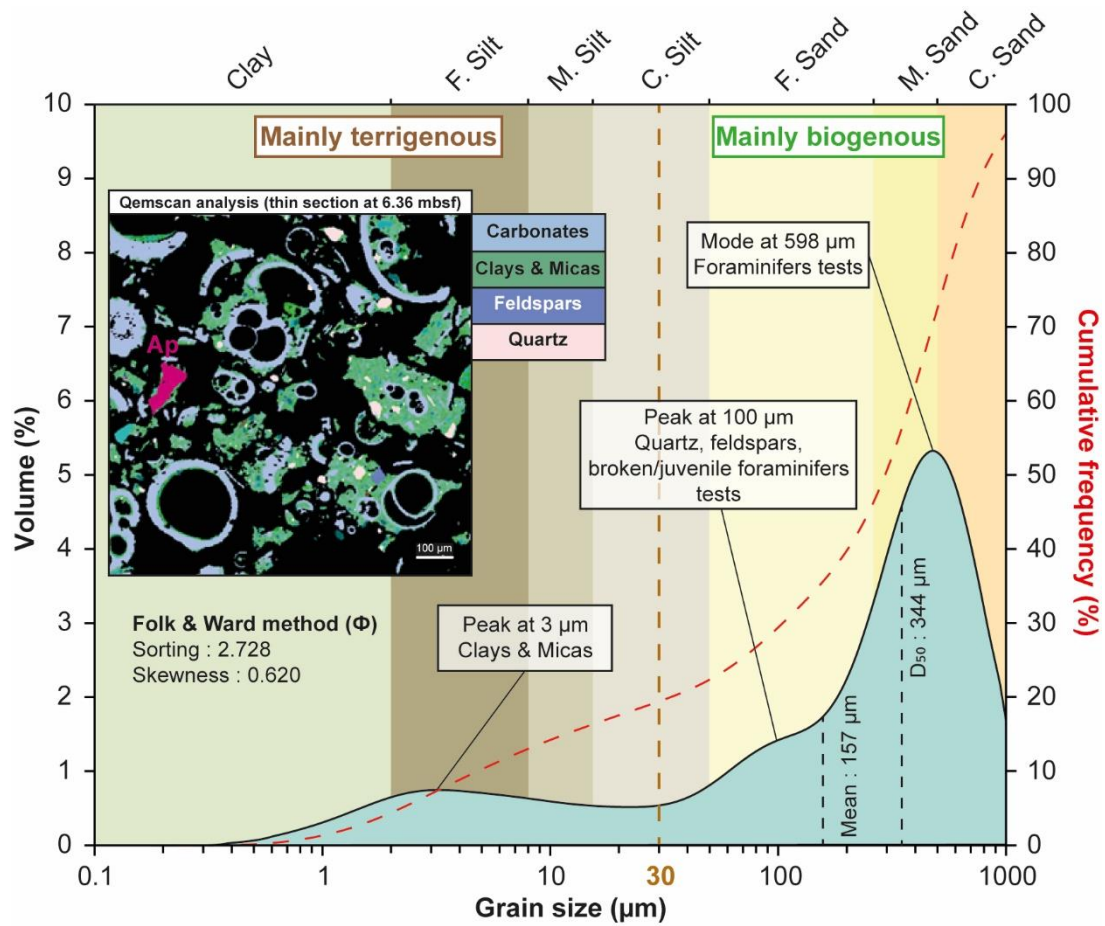


Figure 6. Average grain-size distribution of core MOZ3-CS07, associated cumulative frequency curve and thin section photography analyzed by QEMSCAN. Ap: apatite. The grain size at 30 µm is chosen to separate terrigenous from biogenic particles.

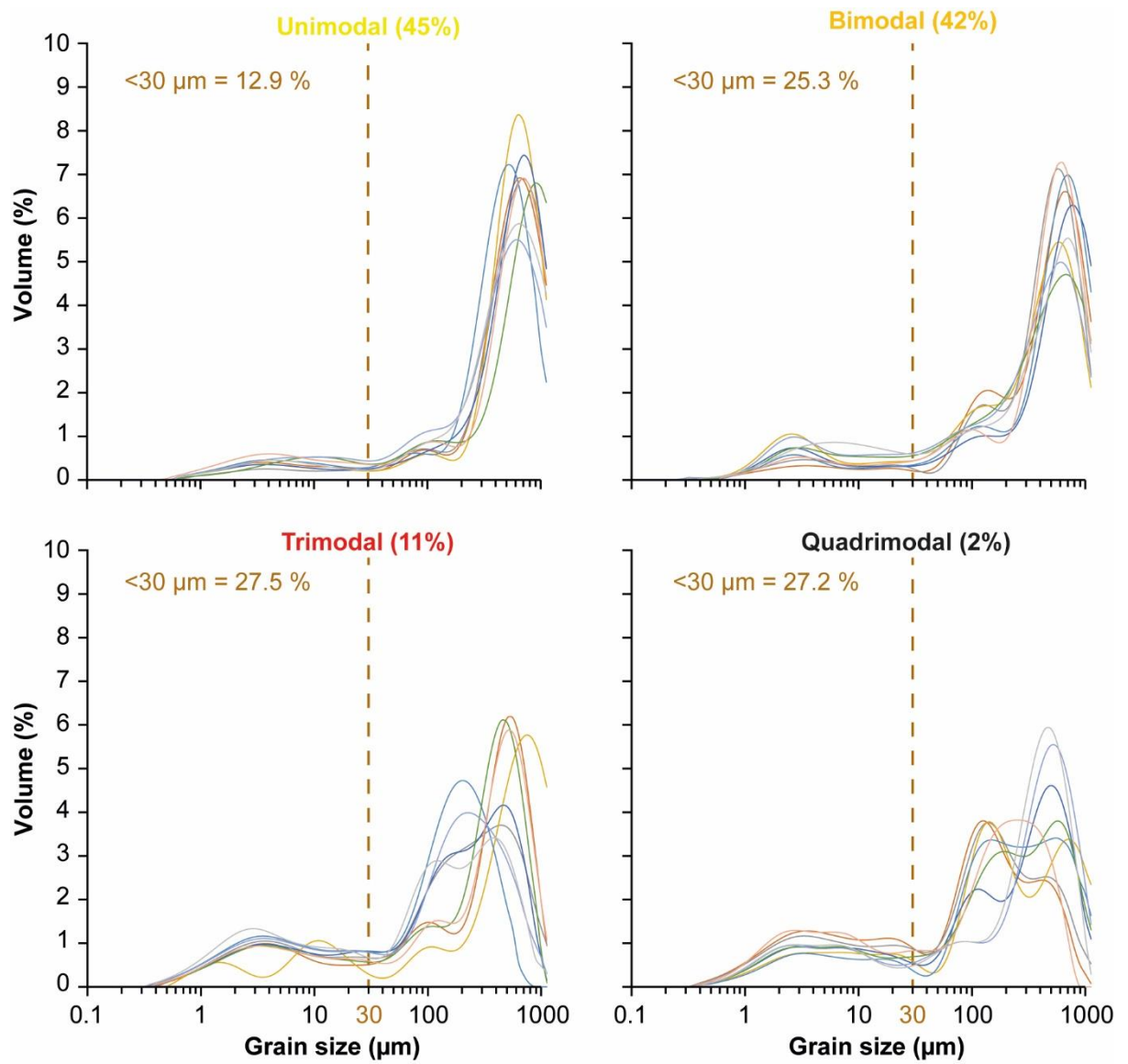


Figure 7. Graphs showing the spectral variability for each type of modal grain-size distribution of core MOZ3-CS07. Each graph gathers the distributions of 9 randomly selected samples. <30 μm correspond to the proportion of the fraction inferior at 30 μm .

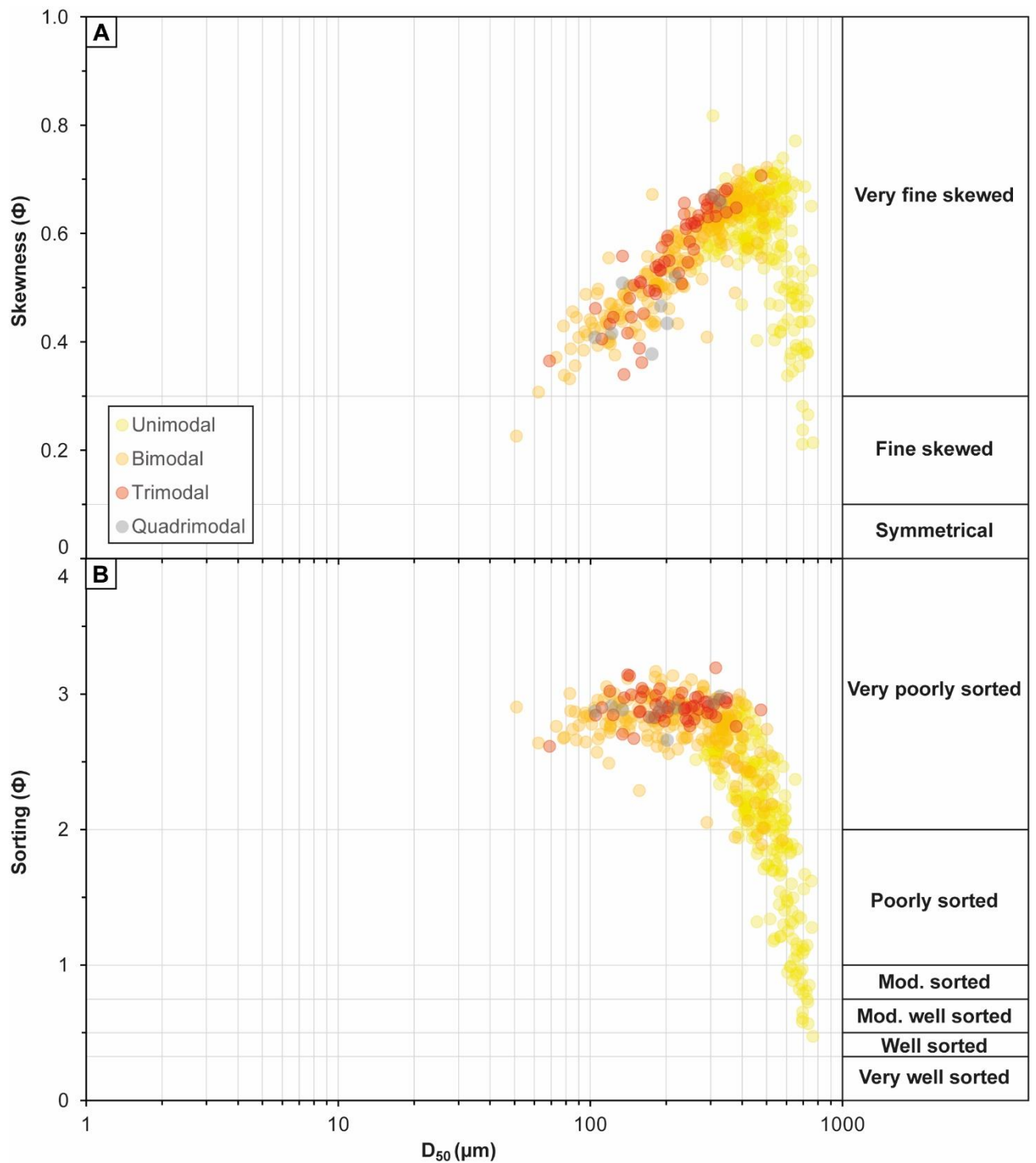


Figure 8. A) Cross-plot skewness (Φ) versus D_{50} . B) Cross-plot sorting (Φ) versus D_{50} , for all the grain-size analysis of core MOZ3-CS07 according to their modal distributions. Unimodal distributions show a different trend than the others with a sediment more symmetrical and better sorted when the grain size increase.

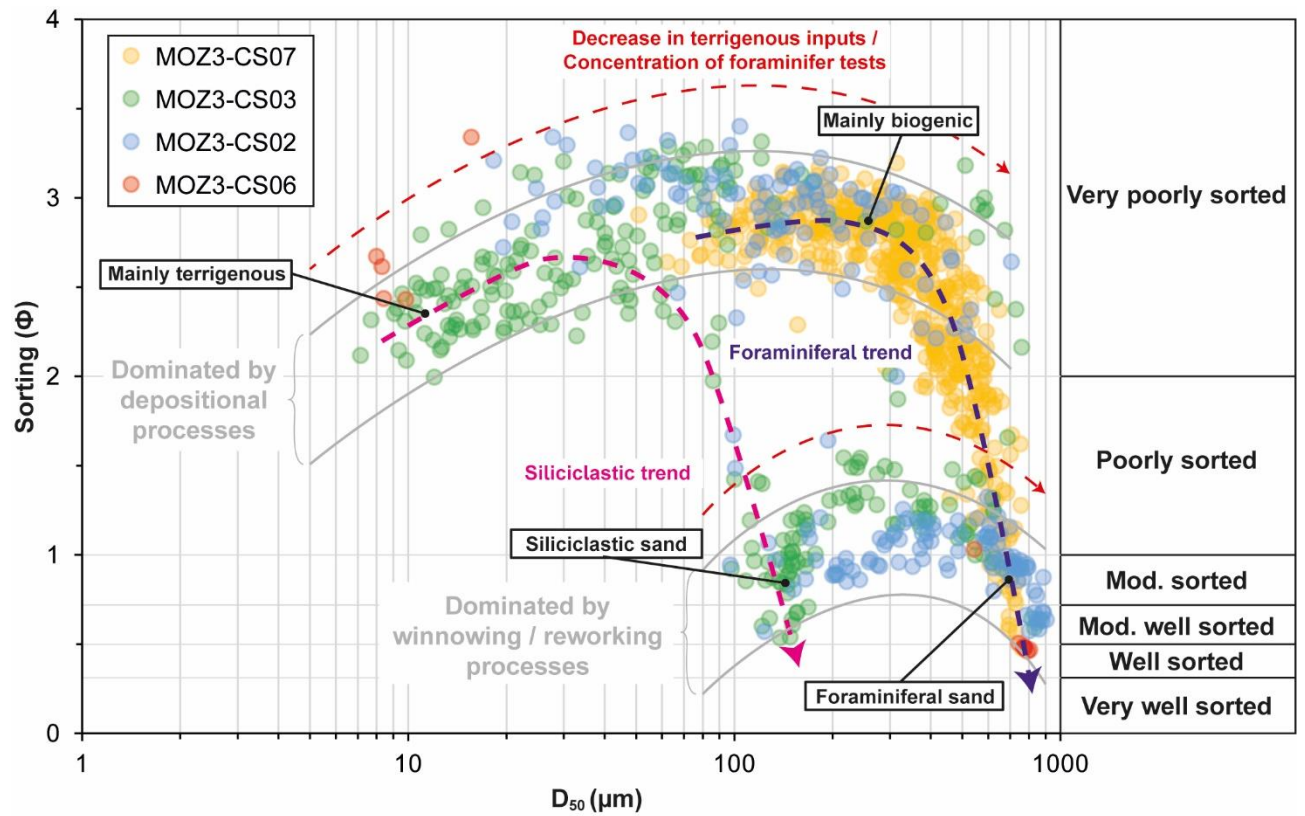


Figure 9. Interpreted cross-plot sorting (Φ) versus D_{50} , for all the grain-size analysis of cores MOZ3-CS03-CS02-CS07 and CS06 (see location in Fig. 2). Four sedimentological poles are identified, gathered into two distinct trends showing the transition from sediments dominated by depositional processes to sediments dominated by winnowing/reworking processes.

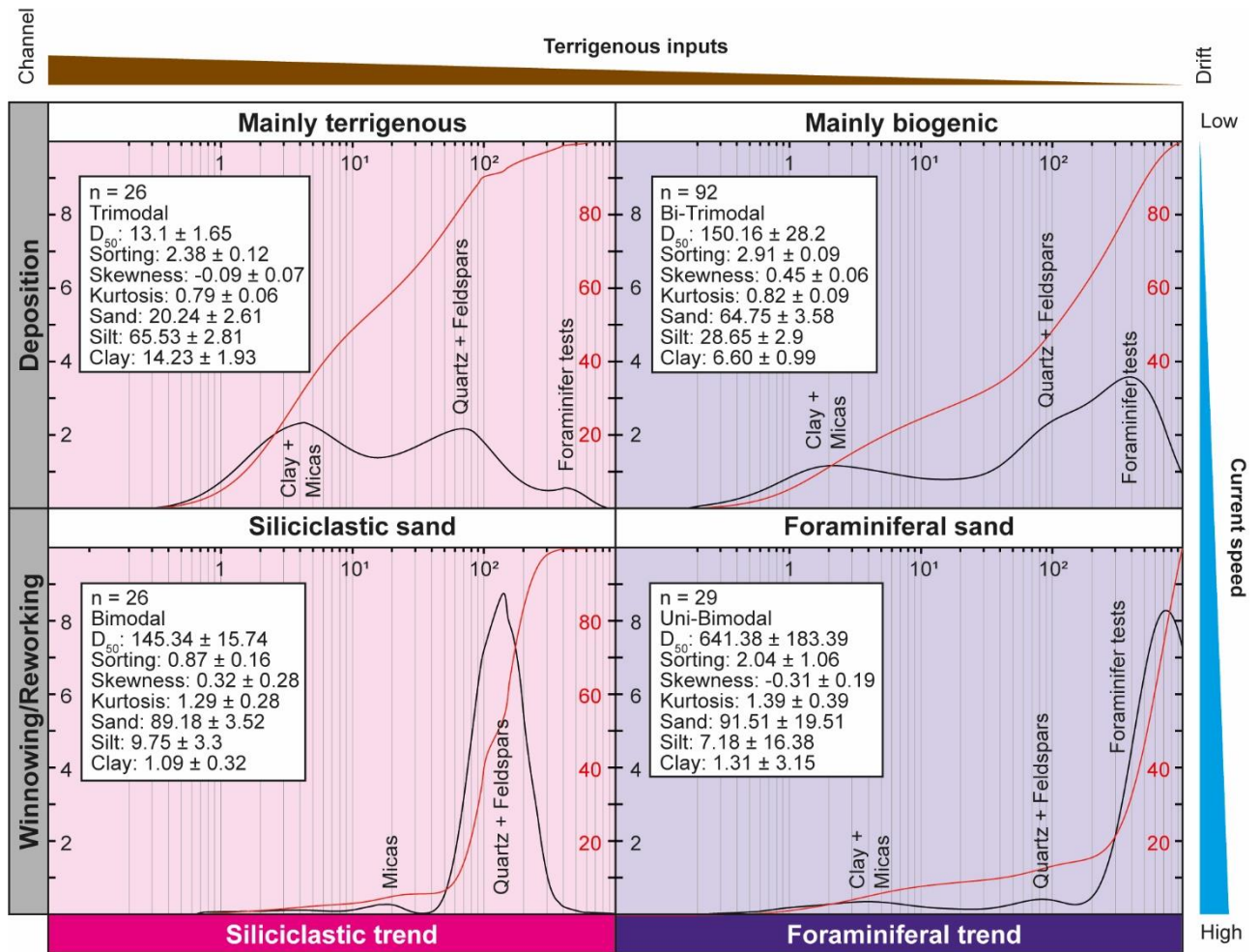


Figure 10. Average grain-size distribution and parameters (Folk and Ward logarithmic method) for each sedimentological pole (Fig. 9), associated their cumulative frequency curves and their interpretation in terms of sedimentary processes, current speed, contourite trends (siliciclastic or foraminiferal) and location in the contourite system. The nature of the modes is based on QEMSCAN analysis. Note that siliciclastic sand and foraminiferal sand grain-size distributions have the same shape but with a shift of the coarsest mode due to the nature of the sediment.

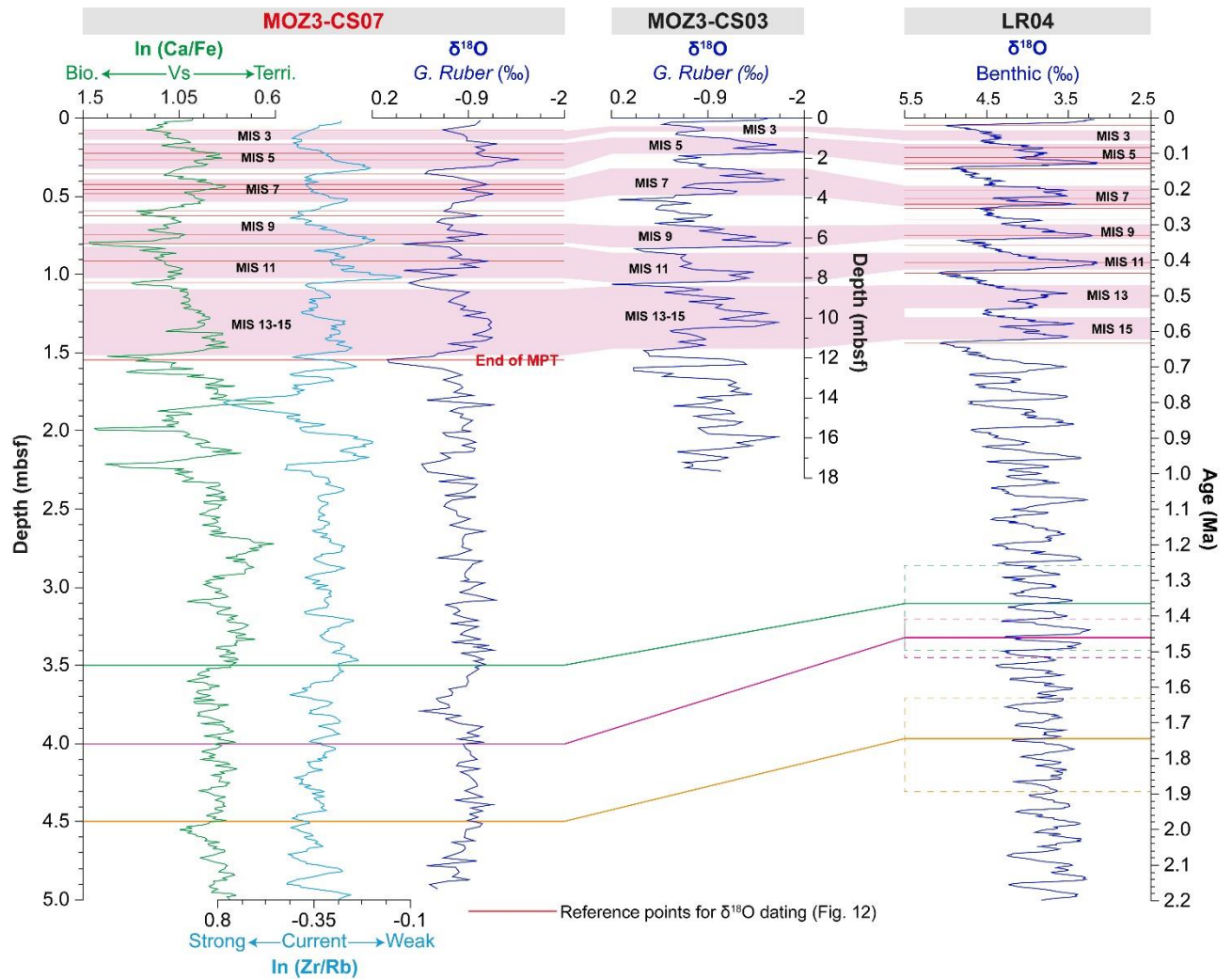


Figure 11. Stratigraphic correlations between the first 5 mbsf of MOZ3-CS07, MOZ3-CS03 and the reference curve LR04 (Lisiecki and Raymo, 2005) using XRF log-ratios (Ca/Fe and Zr/Rb) and $\delta^{18}\text{O}$ measurements. The end of the MPT is estimated at 1.53 mbsf on core MOZ3-CS07 (632 ka). The green, purple and orange lines correspond to strontium isotope measurements and their uncertainties in dashed lines.

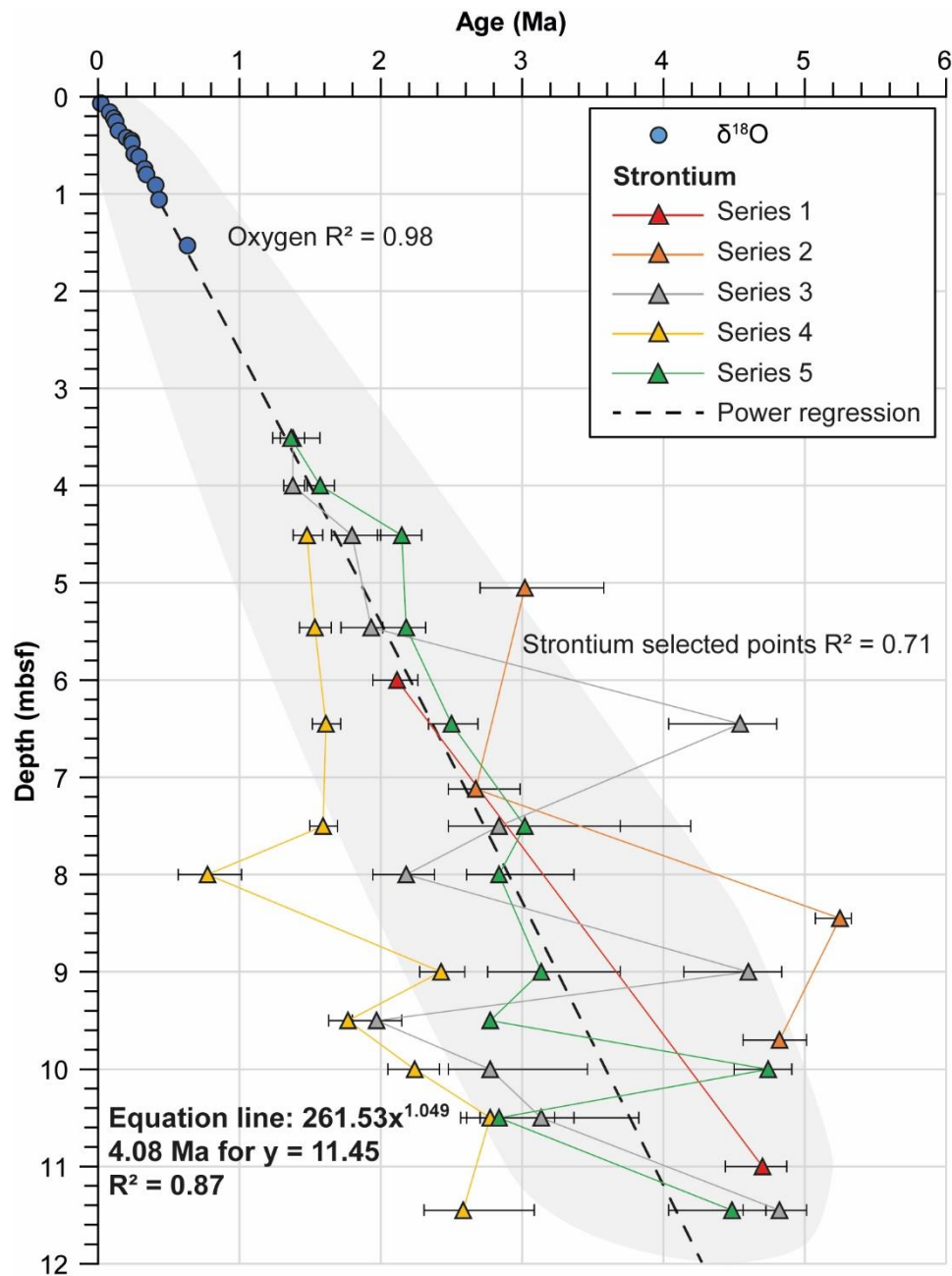


Figure 12. Graph gathering estimated ages from correlations of the $\delta^{18}O$ curve (red lines in Fig. 11) and ages obtained by Sr-Isotope Stratigraphy method for core MOZ3-CS07. The grey area indicates points selected for the power regression. The dashed black line corresponds to the power regression giving an age of 4.08 Ma at the base of the core.

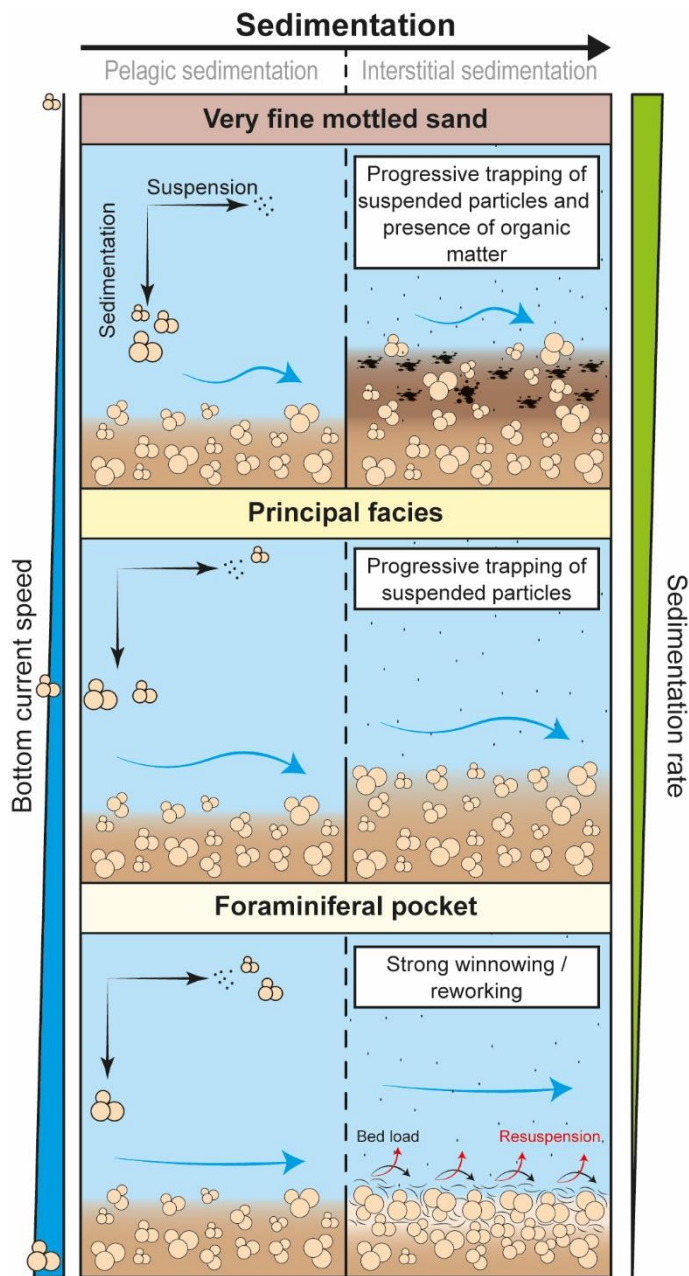


Figure 13. Interpreted sedimentological process at the origin of the foraminiferal sand of core MOZ3-CS07 and its facies variations by interstitial sedimentation.

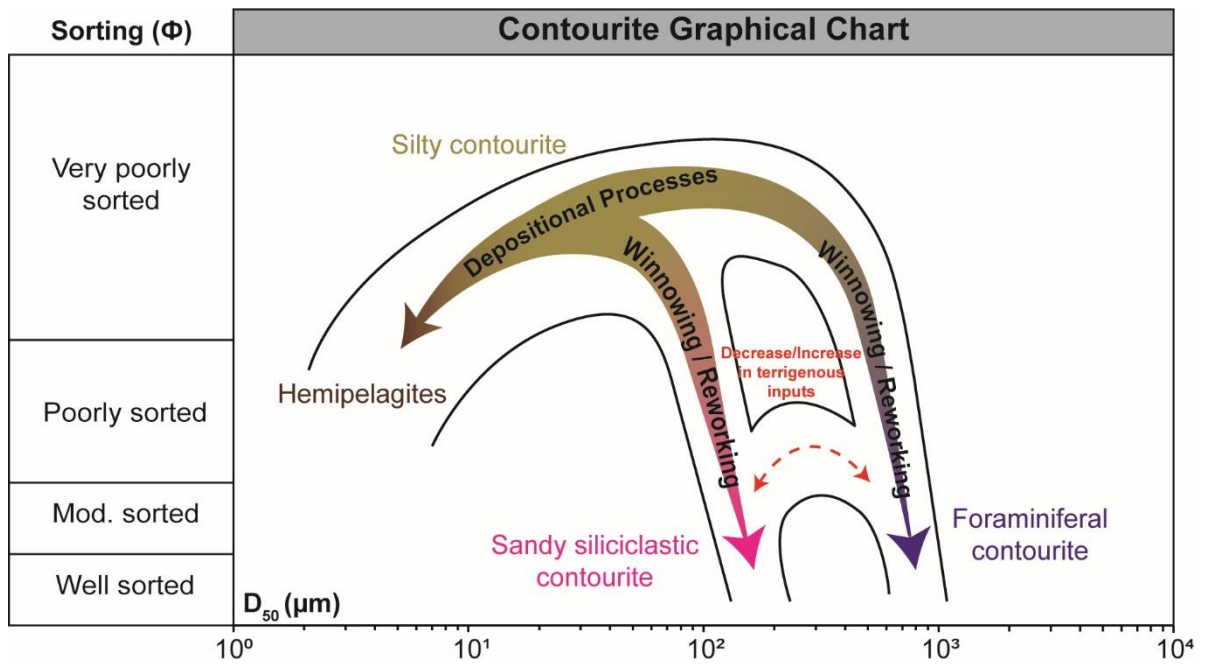


Figure 14. Concept of “Contourite Graphical Chart” corresponding to the preferential location of contourite deposits in cross-plot sorting (Φ) versus D_{50} and the existing continuity between them (inspired from Bankole et al., 2021). Three contourite endmembers are identified.

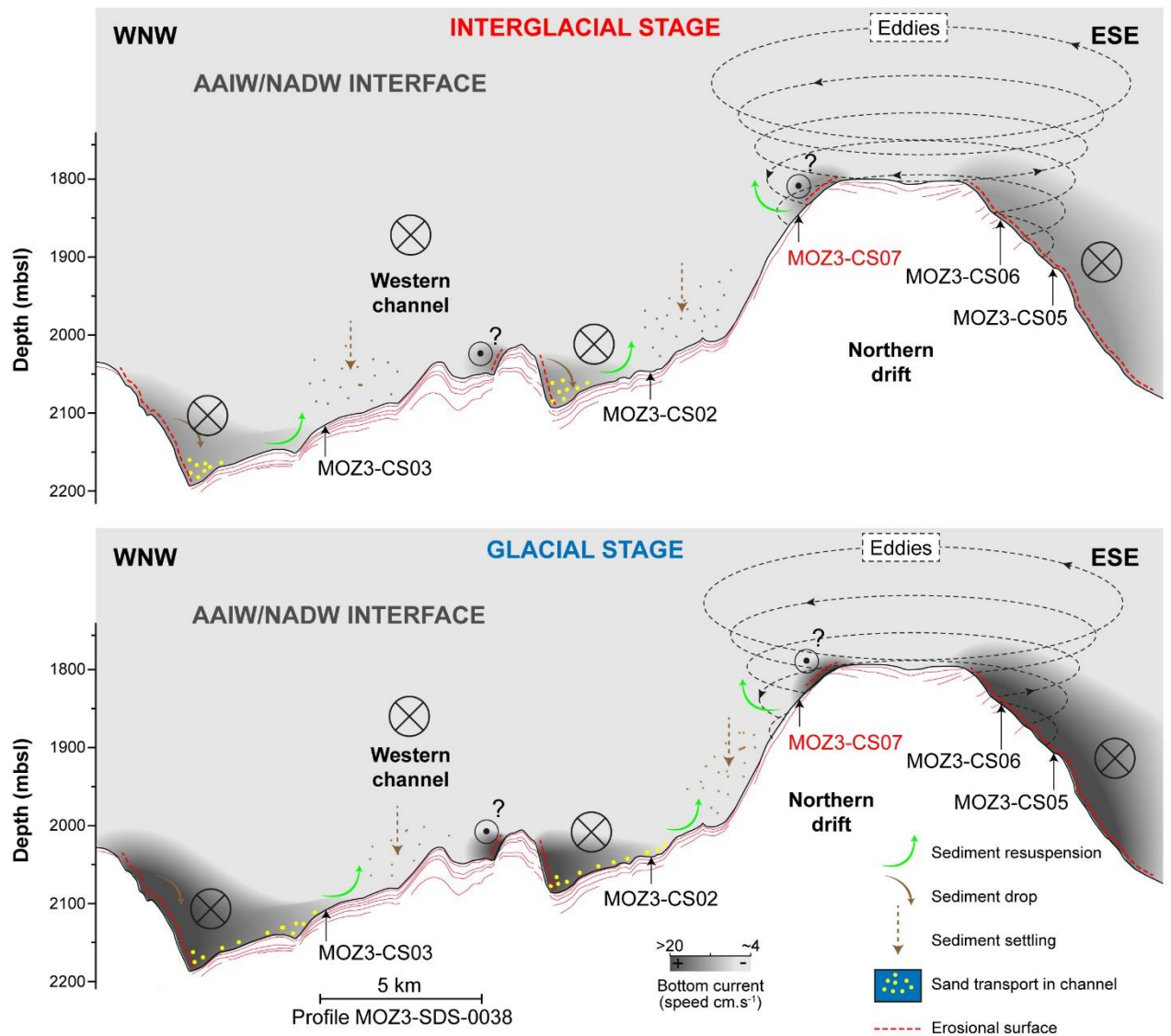


Figure 15. Schematic representation of sedimentary processes, bottom current speed variations over 100 kyr climatic cycles in the AAIW/NADW interface and possible impact of deep anti-clockwise eddies in the contourite system (modified from Babonneau al., 2022). During interglacial stages, bottom current speed is lower than during glacial stages.

14. TABLES

Table 2. List and characteristics of the CALYPSO piston cores collected during the PAMELA-MOZ3 cruise.

Core	Latitude	Longitude	Water depth (mbsl)	Core length (m)	Section number
MOZ3-CS03	S 24° 49.195	E 36° 17.210	2125	20.06	21
MOZ3-CS02	S 24° 52.441	E 36° 25.424	2041	10.66	11
MOZ3-CS07	S 24° 54.129	E 36° 30.192	1853	11.47	12
MOZ3-CS06	S 24° 35.685	E 36° 34.311	1868	7.89	8
MOZ3-CS05	S 24° 56.685	E 36° 35.854	1926	6.35	7

Table 2. Summarize of data acquired on the CALYPSO piston cores. In red are the data previously acquired by Babonneau et al. (2022). Res. = Resolution; MSCL = Multi-Sensor Core Logger; XRF = X-Ray Fluorescence; ^{14}C = radiocarbon dating; $\delta^{18}\text{O}$ = O-isotope measurements (*G. ruber*); $^{87}\text{Sr}/^{86}\text{Sr}$ = Sr-isotope measurements.

Core	Spectrocolorimetry (Res.)	MSCL (Res.)	XRF (Res.)	Mineral composition (No.)	^{14}C (No.)	$\delta^{18}\text{O}$ (Res.)	$^{87}\text{Sr}/^{86}\text{Sr}$ (No.)	Laser grain size
MOZ3-CS03	1 cm	1 cm	1 cm	8	3	10-20 cm	ND	1-7 cm on coarsest parts
MOZ3-CS02	1 cm	1 cm	1 cm	6	ND	ND	ND	1-20 cm
MOZ3-CS07	1 cm	1 cm	1 cm	12	ND	1-4 cm	2 + 38	1-4 cm (27 + 484 analyses)
MOZ3-CS06	1 cm	1 cm	1 cm	ND	ND	ND	ND	12 analyses
MOZ3-CS05	1 cm	1 cm	1 cm	ND	ND	ND	ND	ND

Table 3. Mineral composition obtained on thin sections by QEMSCAN analysis on core MOZ3-CS07.

Depth (mbsf)	Carbonates	Quartz	Feldspars	Clays & Micas	Others
0.33	76,4%	12,5%	4,8%	1,8%	4,6%
1.33	70,7%	20,9%	5,5%	2,4%	0,7%
2.36	62,8%	24,5%	7,8%	3,7%	1,4%
3.33	65,0%	23,7%	7,7%	3,2%	0,6%
4.33	73,3%	16,7%	6,2%	3,5%	0,5%
5.33	64,0%	22,9%	8,7%	3,7%	0,8%
6.33	60,6%	25,8%	10,0%	3,2%	0,5%
7.33	62,2%	24,6%	9,1%	3,7%	0,7%
8.33	66,3%	22,2%	8,1%	2,9%	0,7%
9.33	67,6%	21,4%	7,7%	3,0%	0,5%
10.33	66,5%	18,1%	6,8%	3,4%	5,2%
11.33	69,4%	20,4%	6,9%	2,9%	0,6%
Average	67,1%	21,1%	7,5%	3,1%	1,4%

Table 4. Summarize of strontium series measurements made on core MOZ3-CS07 presented in figure 12. Sigma (σ) correspond to the standard deviation of the 6th decimal. In red are the data previously acquired by Babonneau et al., (2022).

Series	No. of samples	Fraction	Ultrasound	NBS 987 Measured	NBS 987 Standard
1	2	Total	No	0.710248 (2σ)	
2	4	Total	No	0.710272 (3 σ)	
3	12	>250 μm	No	0.710279 (2 σ)	0.710250
4	10	>250 μm	Yes	0.710269 (2 σ)	
5	12	>250 μm	No	0.710267 (3 σ)	